



저작자표시-비영리-변경금지 2.0 대한민국

이용자는 아래의 조건을 따르는 경우에 한하여 자유롭게

- 이 저작물을 복제, 배포, 전송, 전시, 공연 및 방송할 수 있습니다.

다음과 같은 조건을 따라야 합니다:



저작자표시. 귀하는 원저작자를 표시하여야 합니다.



비영리. 귀하는 이 저작물을 영리 목적으로 이용할 수 없습니다.



변경금지. 귀하는 이 저작물을 개작, 변형 또는 가공할 수 없습니다.

- 귀하는, 이 저작물의 재이용이나 배포의 경우, 이 저작물에 적용된 이용허락조건을 명확하게 나타내어야 합니다.
- 저작권자로부터 별도의 허가를 받으면 이러한 조건들은 적용되지 않습니다.

저작권법에 따른 이용자의 권리는 위의 내용에 의하여 영향을 받지 않습니다.

이것은 [이용허락규약\(Legal Code\)](#)을 이해하기 쉽게 요약한 것입니다.

[Disclaimer](#)

February 2019

Master's Thesis

A Study of Thermal and Mechanical  
Characteristics in TIG Assisted Hybrid  
Friction Stir Welded Joints of Dissimilar  
Materials (A15052-DP590) by Numerical  
Analysis

Graduate School of Chosun University

Department of Welding and Joining Science Engineering

Seong-Min Hong

# A Study of Thermal and Mechanical Characteristics in TIG Assisted Hybrid Friction Stir Welded Joints of Dissimilar Materials (A15052-DP590) by Numerical Analysis

수치해석에 의한 TIG-FSW 하이브리드 이종재(A15052-DP590)  
용접부의 열적·기계적 특성에 관한 연구

February 25, 2019

Graduate School of Chosun University  
Department of Welding and Joining Science Engineering  
Seong-Min Hong

# A Study of Thermal and Mechanical Characteristics in TIG Assisted Hybrid Friction Stir Welded Joints of Dissimilar Materials (A15052-DP590) by Numerical Analysis

Advisor: Professor Hee-Seon Bang

A Thesis Submitted for the Degree of  
Master in Engineering

October, 2018

Graduate School of Chosun University  
Department of Welding and Joining Science Engineering  
Seong-Min Hong

*The master's dissertation of Seong-Min Hong was reviewed and approved by the following.*

Chair of Committee:

---

Professor/Ph.D. HanSur Bang

Department of Welding and Joining Science Engineering, Chosun University

Members:

---

Professor/Ph.D. HeeSeon Bang

Department of Welding and Joining Science Engineering, Chosun University

---

Professor/Ph.D. YoonChul Sohn

Department of Welding and Joining Science Engineering, Chosun University

November 2018

Graduate School of Chosun University

# TABLE OF CONTENTS

TABLE OF CONTENTS	1
LIST OF FIGURES	3
LIST OF TABLES	5
ABSTRACT	6

## Chapter I. Introduction

1.1	Background	9
1.2	Characteristics of Fe-Al Intermetallic Compounds (IMC)	13
1.3	Objective	16
1.4	Construction of Thesis	19

## Chapter II. Experimental Development of TIG Assisted Hybrid Friction Stir Welding Process

2.1	Introduction	21
2.2	Experimental Details	24
2.2.1	Experimental Equipment	24
2.2.2	Experimental Method	25
2.3	Optimization of Welding Process	29
2.3.1	Mechanical Evaluation	29
2.3.2	Metallurgical Evaluation	35
2.4	Conclusion	37

## Chapter III. Prediction of Thermal and Mechanical Characteristics of Dissimilar Materials Joints by Hybrid Friction Stir Welding through Numerical Analysis

3.1	Introduction	38
3.2	FE Model of Heat Source for TIG Assisted Hybrid FSW Process	39
3.2.1	Characterization of Heat Source	39
3.2.2	Analysis Method	44

3.2.3	Numerical Model and Welding Condition.....	53
3.3	Thermal Characteristics .....	55
3.3.1	Temperature Distribution.....	55
3.3.2	Fe-Al Intermetallic Compound Layer Thickness.....	65
3.4	Mechanical Characteristics.....	70
3.4.1	Residual Stress.....	70
3.4.2	Plastic Strain.....	75
3.5	Conclusion.....	77

## Chapter IV Summary

Summary.....	79
Reference.....	83
Acknowledgement.....	89

## LIST OF FIGURES

Fig. 1.1	Advantages of vehicle weight reduction .....	9
Fig. 1.2	Comparison between conventional sub-frames and dissimilar materials applied sub-frame of Honda Accord .....	12
Fig. 1.3	Fe-Al phase diagram .....	14
Fig. 1.4	Flow chart of thesis .....	20
Fig. 2.1	Configuration of FSW and HFSW for the experiment .....	24
Fig. 2.2	Schematics of experimental setup .....	26
Fig. 2.3	Schematics of FSW tool .....	27
Fig. 2.4	Schematics of tensile test specimen .....	28
Fig. 2.5	Bead profiles of FSW and HFSW welded joints.....	30
Fig. 2.6	Comparison of tensile strength of FSW and HFSW welded joints.....	31
Fig. 2.7	Comparison of hardness distribution between FSW and HFSW welded joints along the transverse line .....	33
Fig. 2.8	Comparison of axial force in FSW and HFSW welded joints.....	34
Fig. 2.9	SEM-EDS analysis of IMC layer in FSW and HFSW welded joints .....	36
Fig. 2.10	Concentration of Al and Fe in the measured line .....	36
Fig. 3.1	Schematics for vector of rotational speed and travel speed of tool shoulder..	40
Fig. 3.2	Heat generation schematics of FSW tool pin .....	42
Fig. 3.3	Prediction of the IMC layer thickness using temperature history at the joint interface .....	51
Fig. 3.4	Configuration of numerical model for FSW and HFSW welded joints .....	54
Fig. 3.5	Temperature distribution in FSW and HFSW welded joints with welding current of 20, 30, and 40 A .....	56
Fig. 3.6	Sectional view of temperature distribution in Al side along the joint interface .....	57
Fig. 3.7	Longitudinal temperature distribution of the interface from the tool center to TIG in FSW and HFSW welded joints.....	59
Fig. 3.8	Schematics of location for the measurement of the temperature variation along the width direction .....	61
Fig. 3.9	Temperature variation along the width direction in FSW and HFSW welded joints with time .....	61



Fig. 3.10	Schematics of locations for the measurement of temperature history .....	63
Fig. 3.11	Temperature history of FSW and HFSW process .....	64
Fig. 3.12	Schematics of location for the measurement of temperature history in the interface.....	66
Fig. 3.13	Temperature history of the interface in FSW and HFSW welded joints .....	66
Fig. 3.14	The maximum temperature at the interface in FSW and HFSW welded joints.....	67
Fig. 3.15	SEM images of IMC layer in FSW and HFSW process .....	68
Fig. 3.16	Comparison of IMC later thickness between experimental and numerical results.....	69
Fig. 3.17	Distribution of transient welding stress $\sigma_{zz}$ in FSW and HFSW welded joints .....	72
Fig. 3.18	Distribution of welding residual stress in FSW and HFSW welded joints.....	74
Fig. 3.19	Distribution of plastic strain in FSW and HFSW welded joints.....	76

## LIST OF TABLES

Table 1.1	Stability range, crystal structure and hardness of intermetallic compounds formed in Fe-Al binary system at room temperature .....	14
Table 2.1	Chemical compositions and mechanical properties of base materials .....	26
Table 2.2	Chemical composition and dimensions of tool .....	27
Table 2.3	Welding conditions used in the experiments .....	27
Table 2.4	Average tensile strength of FSW and HFSW welded joints.....	31
Table 3.1	Characteristics of contact condition related to tool and matrix velocity .....	41
Table 3.2	Thermo-physical properties of aluminum alloy and steel sheets .....	43
Table 3.3	Welding conditions for dissimilar materials (A1502 to DP590) .....	54
Table 3.4	Estimated IMC layer thickness at the interface .....	67
Table 3.5	Comparison of IMC layer thickness between numerical and experimental results .....	69

## ABSTRACT

### Prediction of Thermal and Mechanical Characteristics in TIG assisted Hybrid Friction Stir Welded Joints of Dissimilar Materials (Al5052-DP590) by Numerical Analysis

Seong-Min Hong

Advisor : Prof. Bang, Hee-Seon, Ph.D.

CO-Advisor : Prof. Bang, Han-Sur, Ph.D.

Department of Welding and Joining Science  
Engineering,

Graduate School of Chosun University

최근 자동차산업 및 각종 수송기산업에서는 승객의 안전과 편의성 향상을 위한 장착부품의 증가와 환경규제에 따른 대응책으로 차체 경량화를 통한 연비향상에 대해 연구가 활발히 진행되고 있다. 경량화 기술 중, 경량금속 및 이종/혼합재료를 채택하는 Multi-Materials Mix Technology의 효율성이 확인됨에 따라 이종재료 접합기술은 위의 연구 중에서도 가장 각광받는 분야이다.

특히, 알루미늄 합금은 기존에 사용되던 스틸에 비해 비중이 1/3 이고, 높은 성형성, 내식성 등을 갖음으로써 그 활용성이 주목을 받고있다. 또한, 고장력강 및 초고장력강은 기존 스틸에 비해 높은 ‘강도 대 중량 비(Strength weight ratio)’ 를

가짐으로써 위의 재료들은 차체 경량화를 위한 최적의 재료로 손꼽히고 있다. 하지만, 기존의 용융용접(Fusion welding)을 이용한 철계(steel) 및 비철계(Al, Mg 합금 등)간의 이종재료 접합은 두 재료의 상이한 물성 차이 및 계면에서 형성되는 취성의 금속간화합물(intermetallic compound, IMC)의 생성으로 견전한 접합부를 얻기 힘들다. 알루미늄합금-초고장력강 용접 시 형성되는 Fe-Al IMC의 경우, 다른 이종재료 용접 시 형성되는 IMC와 달리 형성되는 화합물 모두가 취성의 성질을 나타냄으로써 용접부의 강도를 저하시키는 주요 원인이 된다.

위의 두 접합재료의 물성 차이에서 오는 문제점은 1991년 영국 TWI에서 개발된 고상접합법인 마찰교반접합(Friction Stir Welding, FSW)은 철계와 비철계간의 이종재료 접합에서 모재 대비 약 70~80 %의 접합강도를 확보함으로써 하나의 해결책이 될 수 있다 [1]. 특히, 하이브리드 마찰교반접합(Hybrid Friction Stir Welding, HFSW)은 경질재료(hard material)에 보조열원을 조사하여 재료의 소성유동(plastic flow)을 증가시킴으로써, FSW 단독공정 대비 향상된 접합부 강도를 확보할 수 있으며, 티그(TIG), 레이저, 고주파, 초음파 등 다양한 열원을 보조열원으로 적용한 연구결과들이 보고되고 있다. 최근에는 컴퓨터 하드/소프트웨어의 발달에 의해 이종재료 용접 시 용접부의 온도변화나 열응력, 잔류응력 등의 계산에 대한 상용 프로그램 개발이 활발히 이루어지고 있으며, 이동열원의 효과 및 재료의 온도 의존성을 고려한 열전도, 용접잔류응력 등의 수치해석 기법들이 국내외의 다수 학자들에 의해 활발한 연구와 논문으로 발표되고 있다. 하지만 위의 수많은 노력에도 불구하고, 아직까지 하이브리드 마찰교반 용접을 이용한 알루미늄합금-초고장력강의 용접공정과 수치해석을 이용한 용접 시 형성되는 금속간 화합물(Fe-Al IMC)의 두께 예측에 대한 연구는 미비한 실정이다.

따라서 본 연구에서는 자동차용 부품인 CTR FLR COMPL의 Side Upper TWB 적용을

위한 알루미늄 합금-초고장력강 이종재(AI5052-DP590) 용접부의 신뢰성 확보를 위해 TIG-FSW 하이브리드 용접을 이용한 이종재료 용접공정을 최적화하고, 수치해석 및 금속간화합물(IMC) 예측을 수행하였다. 본 연구에 사용된 재료는 알루미늄합금(AA5052-H32, 2.5t) 및 초고장력강(SFPC590DP, 1.4t)이며, 용접재료의 소성유동 향상을 위한 보조열원은 티그(TIG)를 사용하였다. 보조열원으로 차용된 TIG의 전류(20, 30, 40 A)에 따른 용접부 특성을 평가하기 위해 HFSW 용접부의 특성들은 FSW 단독공정을 이용하여 취득한 용접부의 특성과 비교평가 되었다. 용접에 앞서 실제 시험편과 같은 크기인 250 mm (W) x 600 mm x 2.5 mm (t) 알루미늄 합금 & 1.4 mm (t) 초고장력강의 3차원 유한요소 모델 개발을 통해 용접부의 열전도 해석 및 IMC 두께 예측, 열탄소성 해석을 진행하였다. 수치해석 결과의 신뢰성 확보를 위하여 해석 결과를 실제 실험결과와 비교평가 하였다. Thermocouple을 이용하여 측정된 열 이력을 시뮬레이션과 비교하였으며, 이종재료 TWB 접합부의 기계적 특성 평가를 위해 인장시험 및 Vickers 경도시험을 진행하였다. 접합부의 금속학적 평가는 주사전자현미경(SEM-EDS)을 이용하여 IMC 특성을 고찰하고, IMC의 형성두께를 측정/평가하였다.

수치해석 결과, 예측된 알루미늄 합금-초고장력강 이종재 용접부의 IMC 두께는 1.4 ~ 5.6  $\mu\text{m}$  로 예측되었으며, 이는 실제 평균형성두께인 2.02( $\pm 0.222$ ) ~ 3.94( $\pm 0.518$ )  $\mu\text{m}$  로 유효성이 입증되었다. 예측된 IMC 두께 및 실측 두께는 모두 건전한 용접부 형성조건인 10  $\mu\text{m}$  이하의 두께를 만족하였다. 하이브리드 용접부의 최대 평균인장강도는 TIG 전류 20 A, 용접속도 1 mm/sec, 톨 회전속도 400 RPM의 조건에서 약 184 MPa를 기록하였으며, 이는 알루미늄 모재 강도의 약 84 %로써 FSW 용접부 대비 10 % 향상된 인장강도를 확보할 수 있었다.

# Chapter I.

## Introduction

### 1.1 Background

As regulations on reducing emission gas of vehicles have become a main global issue, improving fuel efficiency is heavily emphasized in the automotive industry. The Corporate Average Fuel Economy (CAFE) requires manufacturers in this industry to achieve the standards of 44.8 miles per gallon (mpg) of fuel efficiency by 2020. The European Council of the European Union have accepted the announcement of CAFE and have agreed to decrease the amount of CO<sub>2</sub> emission within 2020. In this agreement, passenger car standard was decided as reaching 95 g/km (95 %) till 2020, and with 100% compliance in 2021. In terms of light-commercial vehicle standard was decided as 147 g/km for 2020 [2]. In order to respond to these growing demands, the lightweight products have spotlighted as a key solution in vehicle design, because 10% reduction in vehicle weight can lead 6-8% of fuel efficiency improvement as shown in Figure. 1.1.

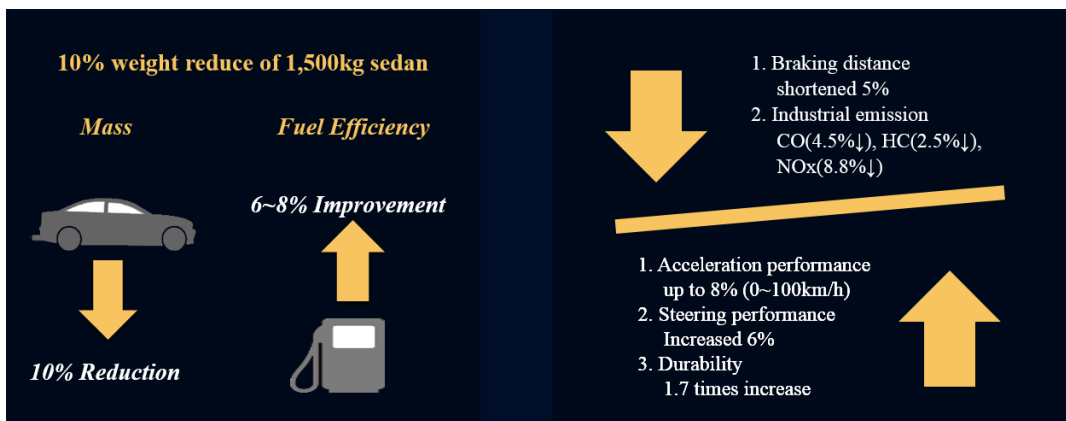


Figure 1.1 Advantages of vehicle weight reduction [3]

The use of lightweight materials, such as instance aluminum (Al) alloy, advanced high-strength steel (AHSS), carbon fiber and polymer composite, and magnesium (Mg) alloy, can be a possible solution to reduce the vehicle body weight and components of chassis up to 50%.

Due to aluminum alloys have high strength-to-weight ratio, automotive industry sees aluminum alloys as the most promising lightweight material in the automotive industry. By adopting aluminum alloys on automobile production, moreover, stiffer and lighter designs can be easily applied into the product in comparison to adopting conventional steels. Especially for automotive components, Al-Mg alloy (AA 5XXX series) is mainly used in chassis as components because of its sound weldability, satisfactory strength and exceptional corrosion resistance. In case of Al-Mg-Si alloy (AA 6XXX series), it is appropriate to be employed in body panels due to its excellent formability and high strength. However, welding steel to aluminum alloy is under an important structural limitation. For example, aluminum alloys' elastic modulus, which is about 70 GPa, is one-third of typical steel, so the Al-steel component would experience a greater deformation in elastic range than the steel-only component under a given load when they have identical size and shape. In addition, aluminum alloys are less formable than automotive steel because of their lower mechanical properties; Aluminum alloys have lower elongation, elastic modulus, plastic strain ratio (r-value) and strain hardening exponent (n-value) that determine the formability of car body and chassis component. Therefore, it is necessary that aluminum alloys should satisfy strength, formability, weldability, and corrosion resistance to be adopted to various automotive parts [4].

For the safety requirement of automobiles, such as crash safety, advanced high-strength steels, such as Complex phase (CP), dual phase (DP), ferritic-bainitic (FB), hot-formed (HF), martensitic (MS), transformation-induced plasticity (TRIP), and twinning-induced plasticity (TWIP) steel, can be adopted with achieving weight reduction simultaneously. Advanced high-strength steel, which has multi-phase microstructure, shows reasonable formability and ductility, but has poor weldability due to its higher carbon and alloying elements than other lower-strength steels. The

higher content of carbon and alloying elements makes advanced high-strength steel on more susceptible welding thermal cycle, resulting in greater variations in microstructures and mechanical properties of welds [5].

As an application of light materials to the vehicle weight reducing, one of the most prominent solutions is multi-material mix technology. Notably, joining aluminum alloy to advanced high-strength steel is increasingly adopted to improve the strength-to-weight ratio of the vehicle components including aerospace, cars, and rails.

The dissimilar materials of steel and aluminum alloy can be joined by adhesive bonding processes, mechanical fastening such as bolting, clinching, and riveting, and thermal joining [6] . However, most of those processes have some drawbacks; adhesive bonding demands long processing time for ensuring effective bonding and causes environmental pollution with their chemical reactions, mechanical fastening process increase stress concentration around the fastened locations [7] . Many states of the art literature also show joining steel to aluminum alloy with conventional fusion welding is significantly restricted due to their significantly different melting temperatures (725 versus 1900 K) and thermo-physical properties like thermal conductivity (238 versus  $77.5 \text{ W}\cdot\text{m}^{-1}\cdot\text{K}^{-1}$ ) and thermal expansion coefficient ( $23.5\times 10^{-6}$  versus  $11.76\times 10^{-6}/\text{K}$ ) between those two materials [8-11]. Additionally, the lower solubility of Al in Fe forms the brittle intermetallic (IMC) layer at the joint interface, but the IMC layer thickness should be optimized to attain sound joint strength and properties [12-15].

As shown in Figure 1.2, Honda Motor Co., Ltd has employed friction stir welding (FSW) process to join dissimilar materials (steel to aluminum alloy) to reduce the sub-frame weight of the Accord 2013 [16] . The success of new joining process for the sub-frame achieved 25% (6 kg) weight reduction than previous process which is mechanical fastening (bolting).



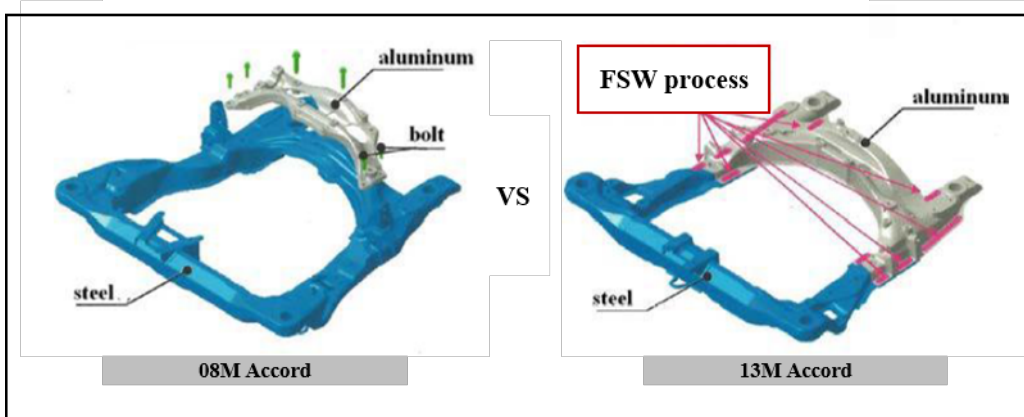


Figure 1.2 Comparison between conventional sub-frames and dissimilar materials applied sub-frame of Honda Accord [16]

Several previous studies recommended the application of hybrid friction stir welding (HFSW) than the conventional friction stir welding (FSW) because the HFSW process not only increases plastic flow of materials which provides improved stirring of FSW tool, but also extends the tool life in joining of harder and high melting point materials like steels [17-20]. In HFSW, an additional heat source is applied in front of the FSW tool to preheat the harder workpiece materials due to the fact that the workpiece at higher temperatures offers improvement of plastic flow and lower resistance which in turn enhances the tool life significantly [15,20-21]. Therefore, a TIG assisted FSW process is used in the present study for joining of aluminum alloy and steel [15].

## 1.2 Characteristics of Fe-Al Intermetallic Compounds (IMC)

As brittle Fe-Al intermetallic compounds (IMC) can deteriorate joint strength of dissimilar materials (aluminum to steel), a comprehensive understanding of characteristics of IMC such as its composition, morphology, nucleation, growth kinetics and mechanism is required to develop the desirable joint.

When dissimilar materials (aluminum and steel) are in contact at elevated temperature, the formation of intermetallic compounds is decided by three main thermodynamic factors. The first is the chemical potentials of aluminum and iron elements, the next is the nucleation conditions at the inter-diffusion process beginning, and the last is the mobility of the alloying constituent during thermal joining process [22]. The Fe-Al phase diagram which is shown in Figure 1.3 depicts the possible formation of Fe-Al intermetallic compounds under the interaction between temperature and element concentration at the atmospheric pressure. Table 1.1 shows crystal structure and hardness for Fig. 1.3. As the intermetallic compounds contain comparatively more Al element, it shows more brittle characteristics than Fe rich intermetallic compounds.

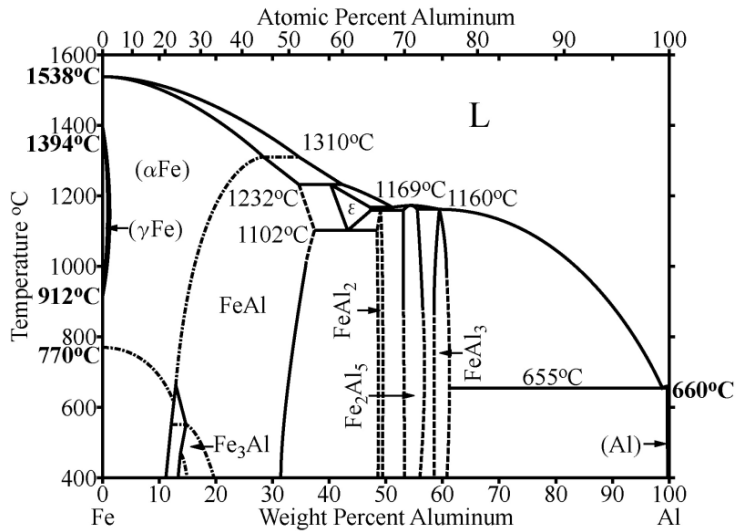


Figure 1.3 Fe-Al phase diagram [23]

Table 1.1 Stability range, crystal structure and hardness of intermetallic compounds formed in Fe-Al binary system at room temperature [22,24]

Phases	Crystal structure	Stability range (at.%)	Vickers hardness (HV)	Density (Mg/mm <sup>3</sup> )
Fe solid solution	BCC	0-45	-	7.8
γ-Fe	FCC	0-1.3	-	7.8
FeAl (β <sub>2</sub> )	BCC (order)	23-55	470-667	5.58
Fe <sub>3</sub> Al (β <sub>1</sub> )	Do <sub>3</sub>	23-34	330-368	6.72
Fe <sub>2</sub> Al <sub>3</sub> (ε)	Cubic (complex)	58-65	-	-
FeAl <sub>2</sub> (ζ)	Triclinic	66-66.9	1058-1070	-
Fe <sub>2</sub> Al <sub>5</sub> (η)	Orthorhombic	70-73	100-1158	4.11
FeAl <sub>3</sub> (θ)	Monoclinic	74.5-76.5	772-1017	3.9
Al solid solution	FCC	99.998-100		2.69

The formation and growth of intermetallic compounds at the joint interface between Al and Fe primarily contain three stages. In the first stage, the formation of solid solution through atomic diffusion is started at the interface. In next stage, nucleation of intermetallic compounds is started when it is thermodynamically more favorable at corresponding temperature and constant pressure. In the third stage, solute atoms will continue to diffuse into the nucleus of stabilized intermetallic compounds for it to grow gradually.

Several studies have been carried out to investigate on growth and characteristics of Fe-Al IMC. The formation of  $\text{Fe}_3\text{Al}$  occurs at a critical temperature of 825 K from FeAl ( $\text{FeAl} \leftrightarrow \text{Fe}_3\text{Al}$ ) while FeAl is formed through a peritectic reaction ( $\text{liquid} + \alpha\text{-Fe} \leftrightarrow \text{FeAl}$ ) under the temperature around 1583K. The Al-rich intermetallic compounds  $\text{FeAl}_3$  are formed easily at a temperature around 1430K through a peritectic reaction ( $\text{liquid} + \text{Fe}_2\text{Al}_5 \leftrightarrow \text{FeAl}_3$ ). The  $\text{Fe}_2\text{Al}_5$  IMC can be formed by congruent compound ( $\text{liquid} \leftrightarrow \text{Fe}_2\text{Al}_5$ ) at a temperature around 1142K. On the other hand, Fe-rich intermetallic compounds with lower aluminum composition, basically FeAl and  $\text{Fe}_3\text{Al}$ , can only be formed at a higher temperature of over 1273 K.

The effects of high pressure raised by the mechanical welding force during FSW also should be considered for the formation of Fe-Al IMC. It was reported that an increase in pressure can lead IMC formation at the interface layer in lower temperature under constant diffusion time. Furthermore, during FSW, materials near the pin are subject to severe plastic deformation at a high strain rate. It is suggested that short-circuiting along static and moving dislocations, grain boundaries and cracks generated during deformation can enhance diffusion and facilitate IMC nucleation by providing heterogeneous nucleation sites.

Above discussions show that the formation and growth of IMCs layers affected by temperature variation, mechanical welding force and material deformation status that are determined by process parameters.

## 1.3 Objective

The purpose of the present study is to investigate the effect of process parameters on growth of IMC layer thickness in TIG assisted FSW of aluminum alloy to steel joints.

A lot of research works on joining aluminum to steel in butt or lap joint by conventional FSW process have been reported. Watanabe et al. [25] noticed tool worn out within a short duration of weld in FSW of 2.0 mm thick AA5083 aluminum alloy to SS400 low carbon steel in butt configuration. The authors reported FeAl and FeAl<sub>3</sub> intermetallic compounds (IMCs) along the joint interface. Tanaka et al. [26] found joint strength decayed exponentially with an increase in Fe-Al IMC layer thickness in FSW of 3.0 mm thick AA7075-T6 aluminum alloy and mild steel. The authors reported the maximum joint strength of 333 MPa when the IMC layer thickness is lower than 0.1 μm. Coelho et al. [14] reported tool pin deformed Al side severely in FSW of 1.5 mm thick AA6181 aluminum alloy and DP690 steel in butt configuration. The authors found a 0.5 mm thick IMC layer of Fe<sub>2</sub>Al<sub>5</sub> along joint interface that yielded the maximum joint strength of 207 MPa, which was nearly 80% of aluminum strength. Liu et al. [27,28] reported tool offset towards aluminum side reduced thrust force experienced by the tool in friction stir butt welding (FSBW) of 1.5 mm thick AA6061 aluminum alloy to 1.4 mm thick TRIP steel. The corresponding IMC layer thickness and the maximum joint strength were reported 1 μm and 196 MPa (~ 70% of aluminum base metal), respectively. Habibnia et al. [29] identified the FeAl<sub>3</sub> and Fe<sub>2</sub>Al<sub>5</sub> IMCs along the interface and reported maximum joint strength of 175 MPa in FSBW of AA5055 aluminum alloy to AISI 304 stainless steel. Wei et al. [30] employed cutting pin in FSW tool to improve the joint strength in FSLW of 3.0 mm thick AA1060 aluminum alloy to 1.0 mm thick SUS321 stainless steel. That study attempted to improve the joint strength by expanding the width of stir zone towards the harder material side. The authors found FeAl<sub>3</sub> IMC along the joint interface and achieved maximum joint strength around 89 MPa. The above studies illustrate tool life is the major problem

in multi-material joining of aluminum alloy to steel by conventional FSW process. Several recent studies are attempted to resolve this issue by employing HFSW process.

Bang et al. [15] preheated the steel plates by TIG arc to reduce the tool wear in HFSW of AA6061 aluminum alloy and stainless steel, both of 3 mm in thickness, in butt configuration. The maximum joint strength in HFSW process was found to be around 290 MPa which was 90% of the aluminum base metal strength. The author achieved higher joint strength in HFSW process in comparison to that of conventional FSW process. In place of TIG arc, several authors used laser beam to preheat the material in FSW process. Bang et al. [21] employed laser beam assisted FSW process to investigate the mechanical characteristic of AA6061 aluminum alloy and DC04 steel joints. The authors concluded that secondary heat source increased the tool life in HFSW by softening the workpiece material prior to progress of the tool. In summary, additional preheat source in HFSW process enhanced both the tool life which consequently improved the mechanical properties of the joint.

Overall, most of the experimental studies have reported Fe-Al IMC layer has a significant effect on joint strength in multi-material joining of aluminum alloy to steel and the excess growth of IMC layer adversely affected the joint strength due to the brittle nature of the intermetallic compounds [13,15,26]. Thus, the a-priori estimation of IMC layer thickness is required to assess the joint strength. Murakami et al. [31] and Das et al. [32] analytically estimated the IMC layer thickness in gas metal arc based joining of aluminum alloy to steel sheet considering parabolic law of diffusion. Crucifix et al. [33] proposed an analytical solution for estimation of the IMC layer thickness using computed temperature histories in friction melt bonding process. At present, very few analytical models are available for estimation of IMC layer thickness. However, no attempts have been reported so far in the open literature for comprehensive modelling in HFSW of aluminum alloy to steel to predict the temperature history and IMC layer thickness as a function of different process conditions in an integrated manner.

In the present work, a coupled experimental and numerical analysis is carried out on TIG

assisted hybrid friction stir welding (HFSW) of 2.5 mm thick A15052 aluminum alloy to 1.4 mm thick DP590 high strength steel plates. The influence of different process parameters on bead quality and growth of the IMC layer are studied extensively. A three dimensional numerical heat transfer model is developed for an a-prior estimation of temperature fields and temperature histories. Further, IMC layer thickness at the joint interface is estimated form numerically analyzed temperature histories and validated the same with the corresponding experimentally measured results.

## 1.4 Construction of Thesis

In Chapter I, research background, objectives and construction of thesis are described.

In Chapter II, experimental researches based on conventional friction stir welding and TIG assisted friction stir welding of 2.5 mm thick Al5052 aluminum alloy to 1.4 mm thick DP590 advanced high-strength steel plates are carried out. This part is mainly focused on the comparison between conventional friction stir welding and TIG assisted hybrid friction stir welding. The influence of different process parameters, which is especially for the effect of preheating source, on the mechanical and metallurgical characteristics of welded joints in dissimilar materials (Al5052-DP590) are investigated in order to guarantee the weldability. For the mechanical and metallurgical characteristics of welded joints in dissimilar materials, bead quality, tensile strength, hardness and growth of the IMC layer are studied.

In Chapter III, numerical simulation research on heat conduction analysis, estimation of IMC layer growth, and elastic-plastic analysis of conventional FSW and TIG assisted hybrid friction stir welding is introduced. This chapter describes temperature distribution, analytical methodology to estimate the growth of IMC layer thickness, and numerically estimated welding residual stress and plastic strain. A heat source model for simulation in transient state thermal conduction analysis is determined considering the conventional FSW and TIG assisted hybrid FSW characteristics. To establish the feasibility of the numerical analysis result, temperature history of the model is compared with that of measured by the thermocouple, and estimated IMC layer thickness is compared with experimentally measured by SEM-EDS. The results obtained from this chapter will be submitted to journal soon.

In chapter IV, knowledge obtained from each chapter is summarized and conclusion is described.

Figure 1.4 shows the flow chart of the thesis which constructs four chapters.



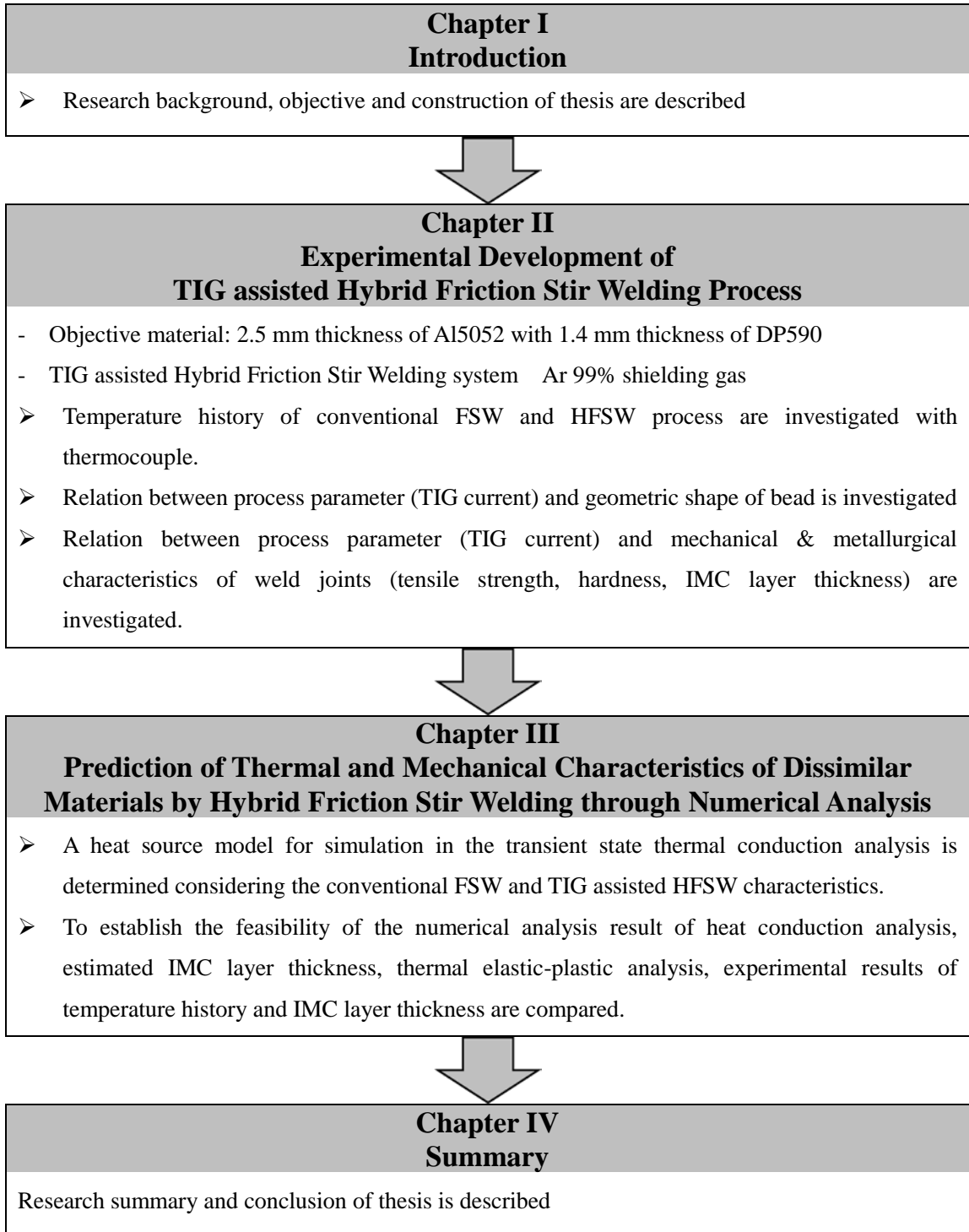


Figure 1.4 Flow chart of thesis

## Chapter II.

# Experimental Development of TIG Assisted Hybrid Friction Stir Welding Process

### 2.1 Introduction

Joining dissimilar aluminum alloy to steel has been getting attentions considerably for lightweight automobile production. However, it is difficult to achieve a sound dissimilar joints by conventional fusion welding because of difference in the solid solubility, thermal properties (thermal conductivity, thermal expansion, heat capacity and melting point), and lattice transformation [34]. In particular, the biggest problem is an excessive formation of intermetallic compound (IMC), which forms due to both chemical reaction and inter-diffusion near interface between aluminum alloy and steel. According to the Fe-Al equilibrium phase diagram [35], non-stoichiometric intermetallic compounds of Fe-rich ( $\text{Fe}_3\text{Al}$ ,  $\text{FeAl}$ ,) and Al-rich ( $\text{FeAl}_2$ ,  $\text{Fe}_2\text{Al}_5$  and  $\text{FeAl}_3$ ) are formed in Fe-Al system. Although Fe-rich intermetallic compound is preferred as ductile phase, Al-rich intermetallic compounds resulting in the brittle joints, are mainly generated in dissimilar joints during welding. Because the presence of intermetallic compound in joints interface can lead to severe problem causing brittleness and low strength, it is necessary that the size and quantity of intermetallic should be properly controlled with lower heat input during welding [36-40].

Many research works in joining of aluminum alloy to steel have been attempted by cold metal transfer welding (CMT), advanced pulsed metal inert gas welding (Advanced Pulsed MIG), resistance spot welding (RSW), laser beam welding (LBM), ultrasonic spot welding (USW) and

friction stir welding [39,41-45]. The primary interest is not only how to control the thickness of intermetallic compounds but also to improve the mechanical properties of the joints. Since the transient thermal cycle and short diffusion time during welding processes may form different intermetallic compounds, an appropriate joining method has been required to join aluminum alloy to steel and to satisfy the strength of dissimilar joints.

Friction stir welding (FSW) developed by The Welding Institute (TWI) in 1991 has become a prominent process for joining of aluminum alloy to steel. The solid-state joining method generates lower heat input as compared to the conventional fusion welding processes preventing solidification problems such as solidification crack and porosity. FSW provides very limited Fe-Al intermetallic compound because the diffusion of Fe and Al in solid phase is much more difficult than the liquid phase. The experimental studies have proven an understanding of the critical issue on joining of aluminum alloy to steel using friction stir butt welding. Watanabe et al. [45] investigated the effects of pin rotation speed, pin offset and pin diameter on tensile strength and microstructure of the dissimilar joints (AA5083 to SS400 mild steel). They obtained maximum tensile strength when pin offset at steel side. Intermetallic compounds of FeAl and FeAl<sub>3</sub> was formed at an upper part of the joint interface, while no intermetallic compounds were observed at central and bottom regions of joint interface. Ramachandran et al. [46] indicated that intermetallic compounds of FeAl, FeAl<sub>2</sub> and FeAl<sub>3</sub> were observed at joint interface and also joint strength was significantly dependent upon the thickness of intermetallic compounds formed at the interface. The typical softening at thermo-mechanically affected zone (TMAZ) close to stir zone (SZ) occurred due to the reduction in dislocation density. However, they explained that as reinforcement, the fragments of steel and intermetallic compounds distributed in the stir zone of aluminum alloy side were contributed to high tensile strength. The effect of tool offset and geometry of tool pin profile on the mechanical and metallographic characteristics of dissimilar joints (Al5052 to HSLA steel) was reported by Ramachandran et al. [47]. Liu et al. [48] quantitatively studied the growth kinetics of interlayer by relationships between thickness and welding speed under process parameters on

rotational speed and tool offset. They indicated that the welding speed was related with interlayer thickness, whereas the variations in rotational speed and tool offset have an effect on the formation of the intermetallic compound of FeAl and Fe<sub>3</sub>Al. Movahedi et al. [49] examined the effect of travel and rotation speed on the formation of reaction layer of dissimilar joints (AA5083 to St-12 steel) to improve the joint quality. They indicated that joint strength was enhanced by decreasing the travel speed and increasing the rotation speed. A thin intermetallic layer of less than 2 μm has no effect on joint strength resulting in fracture of base metal. Dehghani et al. [50] investigated the effect of plunge depth, tilt angle, pin geometry and travel speed at fixed rotation speed on microstructure and tensile strength. As a linear relationship, the thin intermetallic compound layer was formed by increasing travel speed resulting in low heat input.

Tailor welded blanks (TWB), which is combining different thickness materials represents one of the most exciting areas as the lightweight structures in automobile joining applications. Laser beam welding has achieved a relatively significant predominance in the joining of steels [51]. On the other hand, the considerable potential for aluminum joining of TWB with difference thickness has been recently verified by friction stir welding [52]. However, the research work on friction stir welding for tailored welded blanks (TWB) of dissimilar materials with different thicknesses is still not available in the literature for joining of aluminum alloy to steel.

Various aspects, such as such as joining process, joint geometry, sheet thickness, welding distortion and galvanic corrosion relevant to mechanical properties, have to be considered when dissimilar joints are designed for actual application on automotive components [53]. Therefore, the purpose of this study is to assess the applicability of friction stir welding and TIG assisted hybrid friction stir welding for tailored welded blanks of dissimilar materials with different thicknesses. Specifically, a process parameters, effect of TIG current, on mechanical properties and microstructure characterization has been investigated. The side upper of automotive component, where was combined in center floor module, has been manufactured by friction stir welding under optimal conditions obtained in this study.

## 2.2 Experimental Details

### 2.2.1 Experimental Equipment

In the present study, TIG assisted friction stir welding (HFSW) adopting tailored welded blanks with different thickness of dissimilar materials is carried out to join 2.5 mm thickness Al5052-H32 and 1.4 mm thickness DP590 high strength steel. WINXEN FSW gantry type system is coupled with DAIHEN Inverter ELECON 500P TIG welding equipment for hybrid welding experiment. Shielding gas was supplied through a GTAW torch located at 20 mm away from the front of FSW tool. The TIG assisted FSW hybrid welding was implemented, where the TIG arc is perpendicular to the surface of the specimen. Figure 2.1 shows the FSW equipment used in this study in (a) and the set-up for TIG assisted hybrid FSW.



(a) FSW equipment and specification



(b) Experimental setup for TIG assisted hybrid friction stir welding (HFSW)

Figure 2.1 Configuration of FSW and HFSW for the experiment

## 2.2.2 Experimental Method

### (A) Experimental set-up

A 2.5 mm thick Al5052 aluminum alloy and 1.4 mm thick DP590 high strength steel were joined in butt configuration by TIG-assisted FSW process (HFSW). Figure 2.2 shows the Schematics diagram of the experimental setup. Gantry type FSW machine and TIG power source were employed to perform joining. Table 2.1 shows the chemical composition and mechanical properties of the base metals. An 18 mm diameter shoulder with un-threaded taper cylindrical probe was used for the study. Showing Schematics of tool in Figure 2.3, and Table 2.2 shows the chemical composition and dimensions of the tool. The tool tilted an angle of  $3^\circ$  with the vertical axis along the welding direction. The TIG electrode was placed on steel surface in front the FSW tool at a distance of 5.0 mm away from the joint interface, and a standoff distance of 20 mm was maintained between the TIG electrode and FSW tool as shown in Fig. 2.2. Pure argon (99.99%) with a flow rate of 15 l/min was used as a shielding gas to protect the surface from oxidation. The pin was inserted into the aluminum alloy, and pin edge was offset towards steel side at a distance of 0.4 mm from the joint interface to reduce the tool wear. The temperature histories during joining were measured using K-type thermocouples embedded at 1.0 mm and 0.5 mm from top of the aluminum alloy and steel plates, respectively, and at a distance of 16 mm at both sides from the joint interface. Aluminum alloy plates were cleaned with acetone and edges were polished with emery papers before welding to remove the oxide layer.

Table 2.3 shows the processing conditions used in the study. These parameters were selected from preliminary trials. Similar range of welding conditions were also reported in conventional FSW process with an aim to achieve continuous bead along with maximum tensile strength would be more than 45% of the aluminum base metal [15].

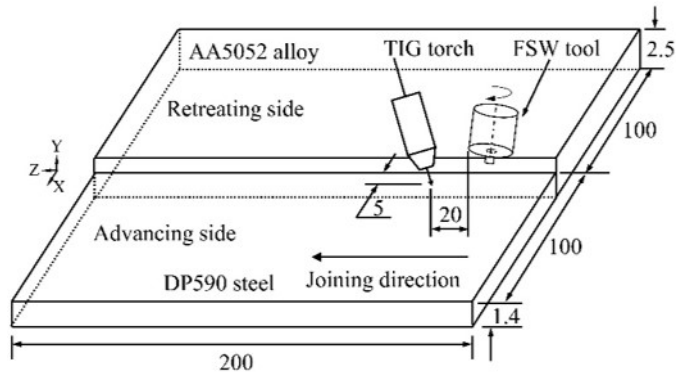


Figure 2.2 Schematics of experimental setup

Table 2.1 Chemical compositions and mechanical properties of base materials

Chemical composition									
Material	Mg	Mn	Zn	Fe	Si	Cr	Cu	Ti	Al
A15052	2.5	0.1	0.1	0.4	0.25	0.15	0.1	0.15	Bal.
Material	C	Mn	Si	S	P	Cr+Mo	Nb+Ti	V	Fe
DP590	0.05	1.2	0.6	0.01	0.06	1.0	0.15	0.2	Bal.
Mechanical properties									
Material	Yield strength (MPa)		Tensile strength (MPa)			Elongation (%)			
A15052	193		220			12			
DP590	459		635			24			

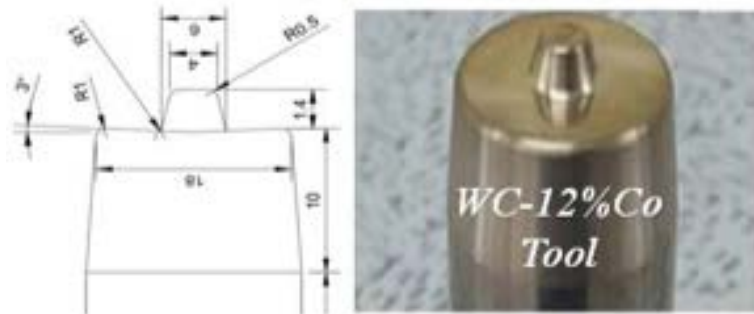


Figure 2.3 Schematics of FSW tool

Table 2.2 Chemical composition and dimensions of tool

Chemical composition	Shoulder diameter (mm)	Pin length (mm)	Pin diameter (mm)	
			Root	Tip
WC-12% CO	18	1.4	6	4

Table 2.3 Welding conditions used in the experiments

Varied parameters					
Case No.	Name set	TIG welding current (A)			
1	FSW	0			
2	HFSW 20 A	20			
3	HFSW 30 A	30			
4	HFSW 40 A	40			
Fixed parameters					
FSW	RPM	Travel speed (mm/sec)	Plunge depth (mm)	Tool inclination (°)	Offset (Al:St)
	400	1	0.8	3	9:1
TIG	Arc length (mm)	Distance to tool (mm)	Distance to interface (mm)	Torch inclination (°)	Shielding gas (%)
	2	20	5	60	Ar, 99.99



## (B) Mechanical test and metallurgical analysis

The bead profiles and corresponding dimensions were examined after polishing and etching with the Keller's reagent. Based on ASTM E8 standard, tensile specimens were tested for each process condition to evaluate joint strength using a universal testing machine (Shimadzu: EHF-EF200kN) at room temperature at a cross head speed of 1 mm/min [54]. Figure 2.4 shows the Schematics of tensile specimens which is oriented along perpendicular to welding direction. The Micro Vickers Hardness (Mitutoyo: AKASHI HM112) was measured along the transverse cross section of welded specimen with a load of 500 g with dwell time of 10 s.

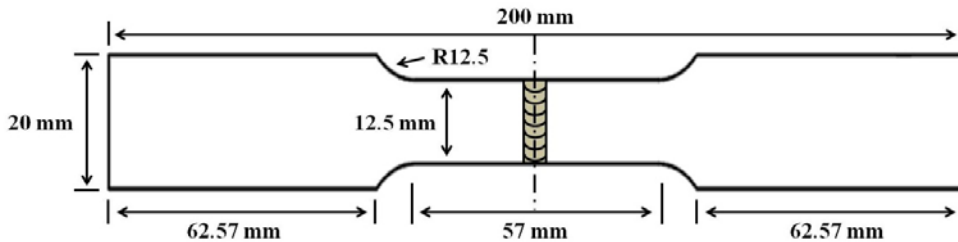


Figure 2.4 Schematics of tensile test specimen

All joint samples for metallurgical observation were polished from SiC paper of 400 to 4000 grit to diamond suspension of 9, 3 and 1 micron. After polishing samples for metallographic, the samples were etched in 5% Nital reagent (100 ml Ethanol+5 ml nitric acid) for 5 s and Tucker's reagent (45 ml HCl+15 ml HNO<sub>3</sub>+15 ml HF+25 ml distilled water) for 10 s to observe the macrostructure through optical microscope (Olympus SZ61 and BX51M with I-solution imaging program). Hitachi S-4800 scanning electron microscope (SEM) combined with X-ray energy dispersive spectroscopy (EDS) was employed to characterize the joint interface and determine the composition of interfacial layer. In addition, the phase of intermetallic compound formed at joint interface was identified by X-ray diffractometer (MODEL) using monochromatic CuK $\alpha$  radiation.

## 2.3 Optimization of Welding Process

### 2.3.1 Mechanical Evaluation

The bead profile of the welded joints by friction stir welding (FSW) and TIG assisted hybrid friction welding (HFSW) under various TIG current as 20, 30, 40 A are shown in Fig. 2.5. When TIG current was increased from 0 A, which is same with conventional FSW process, to 40 A, the width of top bead was increased with wider burr by higher heat input. That could be attributed to the addition of preheating source which in turn increase the temperature and plastic flow of material during HFSW process. Figure 2.5 also shows the cross sectional and back bead profiles of FSW and HFSW welded joints. From the observation of the cross section, it is confirmed that FSW process could not join the dissimilar materials perfectly because of low level of heat input implying the lack of material plastic flow during welding. In contrast, HFSW process showed perfectly joined interface with no defects such as tunnel and crack. As shown in Fig. 2.5, furthermore, the reduction of effective thickness ranging from 2.00 mm to 1.81 mm occurred in the sequence as FSW, HFSW 20 A, HFSW 30 A, and HFSW 40 A welded joints was observed. It is due to the difference of the amount of heat input. The effective thickness of the weld by FSW was most thick among all condition, and that by HFSW 20 A showed slightly thinner thickness. However, in HFSW 30, and 40 A condition, significantly decreased effective thickness were observed. This means the increase of plasticization caused by higher friction heat generation attributes increased temperature by increase in TIG current. From the observation of effective thickness of dissimilar welded joints, it can be inferred that the weld from HFSW 30 and 40 A would have decreased strength by insufficient effective thickness. In all condition, additionally, the steel fragments with irregular shape spread to retreating side (Aluminum alloy side) by stirring action of pin.










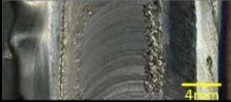

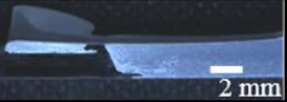
Welding processes	Bead profiles		
	Top	Back	Cross section
FSW		Aluminum  Steel 4mm	 2 mm
HFSW 20 A		Aluminum  Steel 4mm	 2 mm
HFSW 30 A		Aluminum  Steel 4mm	 2 mm
HFSW 40 A		Aluminum  Steel 4mm	 2 mm

Figure. 2.5 Bead profiles of FSW and HFSW welded joints

Table 2.4 and Figure 2.6 shows the comparison of tensile strength of the welded joints of FSW and HFSW with TIG current with 20, 30, 40 A. The average tensile strength of conventional FSW joints and HFSW joints are achieved as 163, 184, 161, and 128 MPa, respectively. The average tensile strength of FSW joints is approximately 163 MPa, whose joint efficiency as approximately 74 % of the Al base metal. The maximum tensile strength of HFSW 20 A processes, on the other hand, are obtained as 187 Mpa. When 20 A of TIG current is adopted, the maximum tensile strength reaches its joint efficiency to 85 % (Average joint efficiency: 84 %) as the preheating source increased plastic flow with higher heat input to the workpiece. However, the average tensile strength has significantly decreased with the increase of TIG current from 30 to 40 A which have excessive heat input inducing thinning effect, as 158 (Joint efficiency: 71 %) and 128 MPa (Joint efficiency: 58 %), respectively.

Table 2.4 Average tensile strength of FSW and HFSW welded joints

Welding Process	Average tensile strength (MPa)
FSW (Case 1)	163
HFSW 20 A (Case 2)	184
HFSW 30 A (Case 3)	158
HFSW 40 A (Case 4)	128

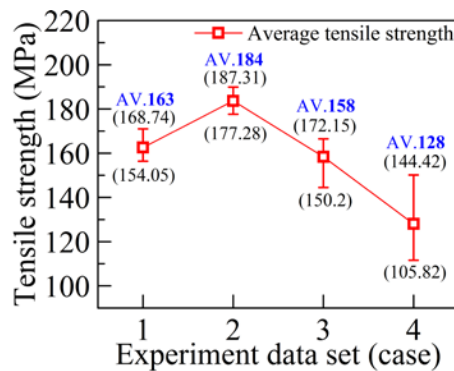


Fig. 2.6 Comparison of tensile strength of FSW and HFSW welded joints

Figure 2.7 shows the hardness distribution measured along the middle line of transverse cross section of conventional friction stir weld and TIG assisted hybrid friction stir weld, which showed the maximum tensile strength when TIG current adopts 20 A. The hardness of base metal Al5052 and DP590 used in this work have ranges of 54-57 HV and 192-198 HV, respectively. The welded joints of HFSW can be divided into four distinct featured zones which are the nugget zone (NZ), thermo-mechanically affected zone (TMAZ), preheating affected zone (PAZ) and base metal zone (BM). For the hardness distribution of HFSW in Fig. 2.7, the minimum hardness value in the nugget zone of retreating side, which is Al side, was about 46 HV. This minimum value indicates lower than the value of the base metal. The W pattern in the nugget zone was observed due to scattered steel particle in the aluminum side. Furthermore, the decrement of hardness value by softening was observed at TMAZ as 5 mm away from joint interface. Similar to the welded joints of FSW, the decrement of hardness value by softening was observed at TMAZ as 2 mm away from joint interface. The softening area of HFSW was wider than that of FSW away from joint interface because of higher heat input. The hardness value of steel side is increased as the location is being close to the joint interface, due to its high hardenability. Compared to the conventional FSW process, the hardness values in HFSW process is increased earlier in preheating affected zone (PAZ) and is being higher than that of FSW process because the presence of preheating source in HFSW allow the steel to experience grain refinement and high hardenability. In the PAZ of the advancing side, especially, the hardness value is increased due to the microstructural; quenching effect after HFSW increase in the martensite and decrease the ferrite matrix. However, the average hardness value in the stir zone of the aluminum side, which is retreating side, was slightly lower than that of the aluminum base metal. The hardness in TMAZ of retreating side close to the stir zone (SZ) shows significantly decreased values. The decrease of hardness value in this area is due to the softening caused by reduction in dislocation density, metallurgical recovery and annealing effect from thermal cycle of FSW process. This phenomenon is also consistent with that of tensile test result indicating fracture of NZ close to the stir zone, which is lower tensile strength.

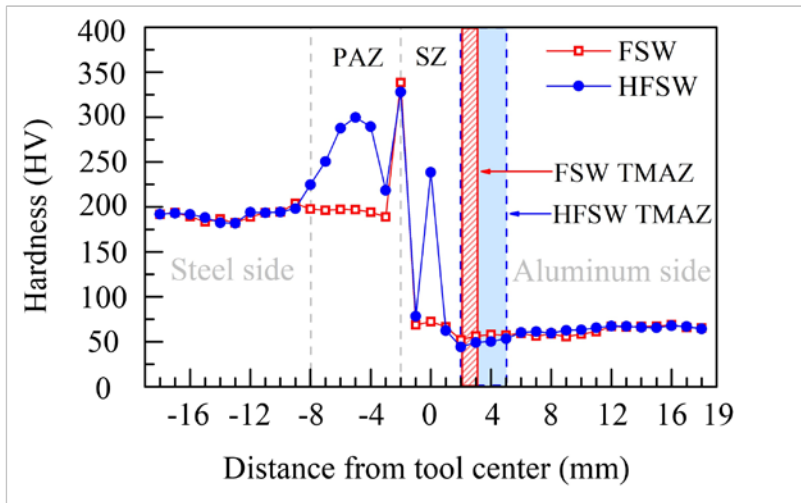


Figure 2.7 Comparison of hardness distribution between FSW and HFSW welded joints along the transverse line

Figure 2.8 shows the effect of preheating source on the axial force ( $F_z$ ) during welding stage of FSW and HFSW under different TIG current of 0, 20, 30, and 40 A. Based on the time- axial force curve depicted in Fig. 2.8, the welding process can be divided into four stages with its distinct feature as plunging stage, dwelling stage, welding stage and pulling stage. Notably, the axial force curve is soared drastically in the plunging stage. After the plunging stage, dwelling stage shows decrease of axial force. Approximately same axial force values in the plunge and dwell stage are shown in the conventional FSW and HFSW, but the lower values of force are obtained in the welding stage as the TIG current increase. Higher heat input from increase of TIG current, which is able to increase the material shear strain rate between the plunged tool surface, especially for pin surface, and material, can reduce the axial force in welding stage. Hence, higher heat input attributes to enhance both plastic material flow and frictional heat generation. As shown in Fig. 2.8, positive correlation is conspicuous between the axial force and TIG current.

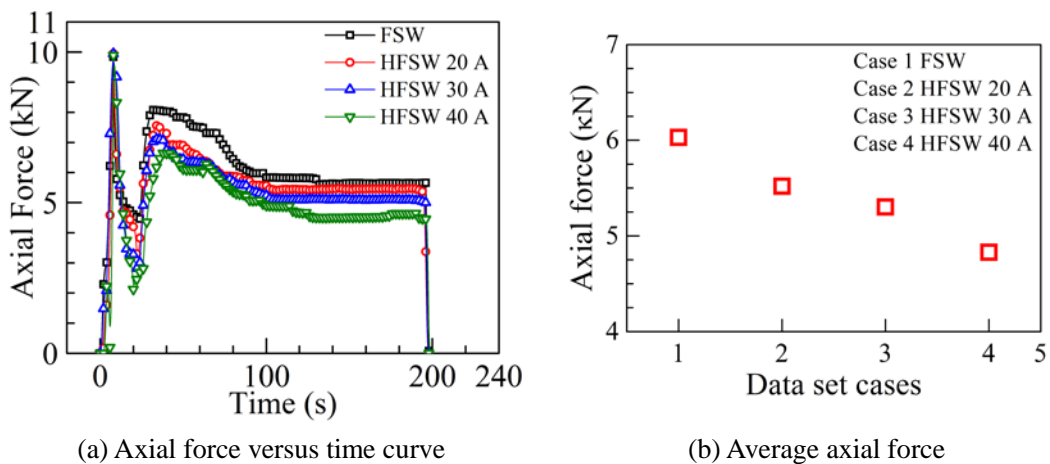


Fig. 2.8 Comparison of axial force in FSW and HFSW welded joints

## 2.3.2 Metallurgical Evaluation

Figure 2.9 shows the SEM macrographs of Fe-Al intermetallic compound (IMC) layer at different welding conditions of FSW and HFSW processes. Left side of the interface indicates steel, while right side is the aluminum alloy. The thickness of the IMC layer were measured at several location along the joint interface and average value was considered. In Figures 2.9 (a) which depicts the IMC layer formation in conventional process, the average value of IMC layer was measured as  $2.02 (\pm 0.2) \mu\text{m}$ . In Fig. 2.9 (b) to (d), measured IMC layer thickness in HFSW with TIG current 20, 30, and 40 A show the average values as 2.77, 3.18, and  $3.94 (\pm 0.5) \mu\text{m}$ , respectively. The increase of IMC layer can be attributed to the higher amount of heat generation at high TIG pre-heat source current. The morphology of the IMC layer was serrated type and oriented towards the aluminum alloy side that implied non-uniform diffusion between Fe and Al at the interface. Furthermore, EDS with line analysis is used to observe the composition of the IMC layer and to identify the variation of the chemical compositions of the available elements along the layer thickness. Figure 2.11 shows the concentration in weight percentage of Fe and Al elements along the IMC layer for HFSW weldments with TIG welding current of 40 A. Figure 2.10 shows the concentration of aluminum and steel is increasing and decreasing from the base metal to the joint interface, respectively. The concentration in weight percentage of aluminum and steel along the IMC layer is varied from 7 ~ 23% (67 ~ 92 at%) and 1 ~ 9% (23 ~ 3 at%), respectively. The variation of Fe and Al concentration in IMC layer indicates there is possibility to form various intermetallic compounds. Substituting the concentration of the Al and Fe elements of Figure 2.10 into Fe-Al binary phase diagram, it is confirmed that the formation of Al-rich intermetallic compounds such as  $\text{Fe}_2\text{Al}_5$  and  $\text{FeAl}_3$  would be formed easily.



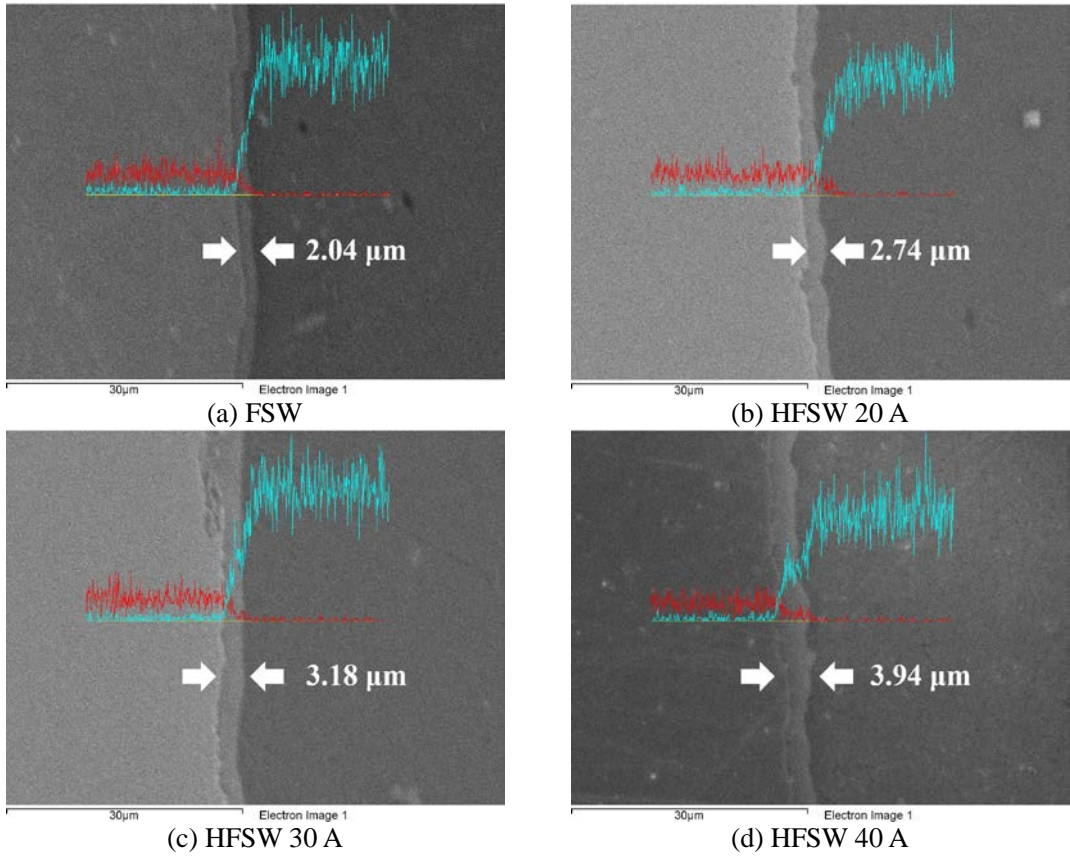


Figure 2.9 SEM-EDS analysis of IMC layer in FSW and HFSW welded joints

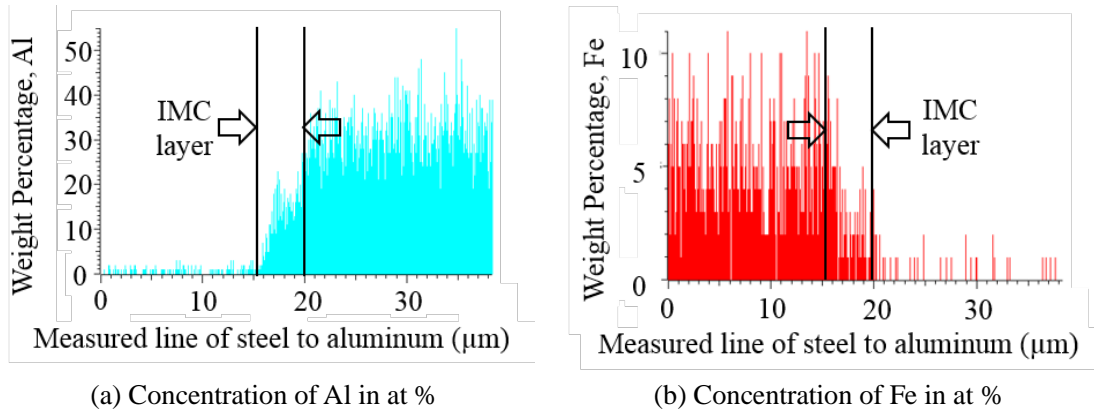


Figure 2.10 Concentration of Al and Fe in the measured line

## 2.4 Conclusion

Fixing the welding conditions as travel speed as 1 mm/s, tool rotational speed as 400 RPM and varying TIG current from 0 to 40 A, dissimilar joining of different thicknesses with 2.5 mm thick Al5052 and 1.4 mm thick DP590 steel has been successfully achieved by TIG assisted Hybrid Friction Stir Welding (HFSW) in the present study. The results can be summarized as follow:

- Compared to the welded joints of conventional FSW, the welded joints of HFSW which adopts 20 A of TIG current shows the perfectly welded joints and indicates the optimum welding condition with no internal or external defect. The highest average tensile strength is achieved as 184 MPa (Joint efficiency: 84 %), and this strength is 10 % increased value than the tensile strength of the joint of conventional FSW due to the increased material plastic flow by preheating source TIG. In both welded joints of FSW and HFSW 20 A, In addition, the localized decrement in hardness value at TMAZ of the aluminum side, which is retreating side, close to stir zone is observed due to the softening caused by reduction in dislocation density, metallurgical recovery and annealing effect during thermal cycle.
- The effect of preheating source, TIG, also shows that the axial force to the tool is decreased as increased heat input prompts the material flow in the harder material (steel).
- From the results of SEM-EDS analysis, the intermetallic compounds (IMC) layer thickness formed by FSW was approximately 2.04  $\mu\text{m}$ , while that by HFSW were 2.77  $\mu\text{m}$ . The IMC layer thickness is increased as the rate of temperature variation is increased by the preheating source. Consequently, the elevated temperature by TIG, significantly affects the growth of IMC layer, and the thickness satisfied under 10  $\mu\text{m}$  thickness standard for the application in the industrial field.

## Chapter III.

# Prediction of Thermal and Mechanical Characteristics of Dissimilar Materials Joints by Hybrid Friction Stir Welding through Numerical Analysis

### 3.1 Introduction

The state of the art literature shows that aluminum alloy to steel joining is mainly restricted due to their considerable gap of melting temperatures and thermo-physical properties [8-10]. The lower solubility of Al in Fe induces the formation of intermetallic (IMC) which is brittle layer at the joint interface [12,13]. The presence of IMC layer is unavoidable in joining aluminum to steel, but the IMC layer thickness has to be optimized to achieve desirable joint strength and properties [13-15]. Preceding studies recommended the application of hybrid friction stir welding (HFSW) rather than the conventional friction stir welding (FSW) because of its higher plastic flow inducement during the welding process and the longer tool life in joining of harder and high melting point materials like steels [17-20]. In HFSW, an additional preheating heat source is applied to the harder workpiece materials prior to progress of the tool due to the fact that the workpiece at higher temperatures offers an environment to promote plastic flow and lower resistance which in turn enhances the tool life significantly [15,20,21]. Therefore, a TIG assisted FSW process is used in the present study for joining of aluminum alloy and steel [15].

The purpose of the present study is to investigate the effect of process parameters on growth of IMC layer thickness in TIG assisted Hybrid FSW of aluminum alloy to steel joints. In the present work, numerical and experimental analysis are carried out on TIG-assisted HFSW of 2.5 mm thick Al5052 aluminum alloy to 1.4 mm thick DP590 high strength steel plates. The different

process parameters to heat conduction analysis, growth of the IMC layer, and thermal elastic-plastic analysis are studied. A three dimensional numerical heat transfer model is developed to estimate the temperature fields, temperature histories, residual stress, and plastic strain. Further, IMC layer thickness at the interface is estimated from numerically analyzed temperature histories and validated the same with the corresponding experimentally measured results.

## 3.2 FE Model of Heat Source for TIG Assisted Hybrid FSW Process

### 3.2.1 Characterization of Heat Source

#### (A) Heat Generation of FSW

The heat energy is generated by frictional heat and deformation at the interface between the tool shoulder and workpiece, and at the interface of tool pin and workpiece during friction stir welding process. For three-dimensional numerical modeling on heat generation in conventional friction stir welding (FSW), the total heat generation is simply expressed as follow:

$$Q_{total} = Q_{shoulder} + Q_{pinsurface} + Q_{pinbottom} \quad (3.1)$$

At a steady state, one-dimensional heat flow through the interface of two metallic materials, the estimation for percentage of heat transferred to the workpiece ( $\eta_h$ ) is as following

$$\eta_h = \frac{\sqrt{(K \times \rho \times C_p)_{W_0}}}{\sqrt{(K \times \rho \times C_p)_{T_0}} + \sqrt{(K \times \rho \times C_p)_{W_0}}} \quad (3.2)$$

where the  $W_0$  and  $T_0$  refer to workpiece and tool material, respectively. The equation assumes an intimate contact between the tool and the workpiece, and a constant thermos-physical properties.

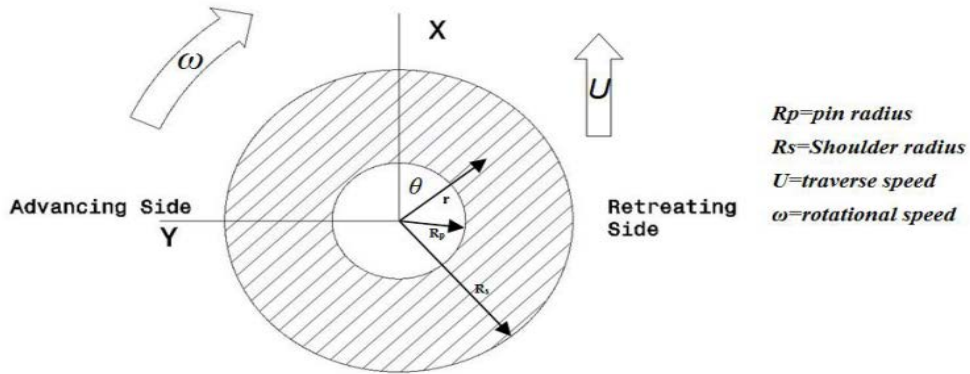


Figure 3.1 Schematics for vector of rotational speed and travel speed of tool shoulder

When the extent of slip; sticking condition is  $\delta = 1$ , no material stick to the tool and all heat is generated by friction. On the contrary, when sticking condition is  $\delta = 0$ , which can be refer to total slip, all heat is generated by plastic deformation. The detailed characteristics of tool-workpiece contact conditions and matrix velocity are shown in Table 3.1. The terms on extent of slip ( $\delta$ ) and coefficient of friction ( $\mu_f$ ) are estimated as below [55,56]

$$\delta = -0.026 + 0.5 \times \exp\left(\frac{\omega r}{1.87}\right) \quad (3.3)$$

$$\mu = 0.51 \times \exp(-\delta \omega r) \quad (3.4)$$

As shown in Fig. 3.1, the tangential speed ( $V_r$ ) of the tool with regard to the workpiece between the tool shoulder and workpiece interface can be described as following,

$$V_r = (\omega r - U \sin \theta) \quad (3.5)$$

The local heat generation rate ( $q_1$ ) due to friction at shoulder-workpiece interface is shown as,

$$\begin{aligned} q_1 &= \delta \times V_r \times \mu_f P dA \text{ (sliding velocity} \times \text{frictional force)} \\ &= \delta \times (\omega r - U \sin \theta) \times \mu_f P dA \end{aligned} \quad (3.6)$$

The local heat generation rate ( $q_2$ ) from the shear deformation at shoulder-workpiece interface is expressed as following,

$$q_2 = \eta_m \times (1 - \delta) \times (\omega r - U \sin\theta) \times \tau_y dA \quad (3.7)$$

Table 3.1 Characteristics of contact condition related to tool and matrix velocity

Contact condition	Matrix velocity (m/sec)	Tool velocity (m/sec)	Shear stress (Pa)	State variable
Sticking	$v_{\text{matrix}} = v_{\text{tool}}$	$v_{\text{tool}} = \omega r$	$\tau_{\text{friction}} > \tau_{\text{yield}}$	$\delta = 1$
Sticking/sliding	$v_{\text{matrix}} < v_{\text{tool}}$	$v_{\text{tool}} = \omega r$	$\tau_{\text{friction}} \geq \tau_{\text{yield}}$	$0 < \delta < 1$
Sliding	$v_{\text{matrix}} = 0$	$v_{\text{tool}} = \omega r$	$\tau_{\text{friction}} < \tau_{\text{yield}}$	$\delta = 0$

Due to friction and plastic deformation between rotating tool and workpiece at the interface, these two components on equations 3.6 and 3.7 can be summing up, and the rate of heat generation per unit area along the tool shoulder and workpiece interface ( $Q_s$ ) is calculated as below,

$$Q_s = \eta_h \frac{q_1 + q_2}{dA} = \eta_h [\delta \mu_f P_N + \eta_m (1 - \delta) \tau_y] (\omega r - U \sin\theta) \quad (3.8)$$

where  $\eta_h$  is heat partition efficiency,  $\delta$  is extent of slip,  $\mu_f$  is coefficient of friction,  $P_N$  is axial pressure,  $\eta_m$  is mechanical efficiency,  $\tau_y$  is the temperature dependent shear yield stress of the deforming material,  $\omega$  is the rotational speed,  $r$  is the radial distance from the tool axis and  $U$  is the welding speed.

As shown in Fig. 3.2,  $R(z)$  is linearly decreased from the top to bottom surface of the tool pin and can be expressed as following,

$$R(z) = R_1 + (R_2 - R_1) \frac{z}{h} \quad (3.9)$$

Because of plastic deformation in workpiece by tool pin, the rate of heat generation around the workpiece region vertical to the taper pin is applied as volumetric heat intensity ( $Q_{ps}$ ), and is calculated as below [56],

$$Q_{ps} = \eta_h [\eta_m (1 - \delta) \tau_y + \delta \mu_f \sigma_y] \{ \omega R(z) - U \sin \theta \} \left( \frac{A_i}{V_i} \right) \quad (3.10)$$

where  $\eta_h$  is the percentage of heat transferred to the workpiece.  $\eta_m$  is the mechanical efficiency, which is a material dependent parameter on complex function of strain, strain rate and temperature. The temperature dependent shear yield strength of workpiece ( $\tau_y$ ) was considered as  $\sigma_y / \sqrt{3}$ , where  $\sigma_y$  represented yield strength based on Von Mises yield criteria [55].  $\sigma_y$  and  $R(z)$  are the temperature dependent yield strength of the deforming material and pin radius, respectively.  $A_i$  and  $V_i$  are the pin surface contact area and the volume of the presumed shear layer adjacent to the pin surface.

The rate of frictional heat generation along the pin bottom surface is applied as volumetric heat intensity by multiplying the rate of heat generation per unit area along the tool shoulder and workpiece interface ( $Q_s$ ) with below [57,64],

$$Q_{pb} = \eta_h [\eta_m (1 - \delta) \tau_y + \delta \mu_f \sigma_y] \times \{ \omega r - U \sin \theta \} \times \left( \frac{A_i}{V_i} \right) \quad (3.11)$$

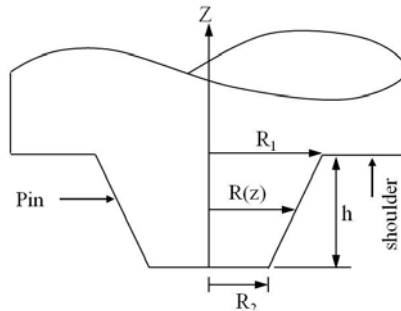


Figure 3.2 Heat generation schematics of FSW tool pin

## (B) Heat Generation of TIG

In TIG assisted HFSW process, heat input form TIG electrode was considered as a surface heat flux as [55]

$$q_{s2} = \frac{d\eta P_w}{\pi r_{eff}^2} \exp\left(-d \frac{x^2+y^2}{r_{eff}^2}\right) \quad (3.12)$$

where  $d$  was the energy distribution coefficient,  $\eta$  and  $P_w$  referred to process efficiency and arc power, and  $r_{eff}$  represented effective radius of TIG arc on top surface of the workpiece. The values of  $d$  and  $\eta$  were considered as 1.3 and 0.5, respectively. A lumped heat transfer coefficient of  $h_0(T - T_0)^{0.25}$  was considered to represent the heat loss from bottom surface where  $h_0=70$  W/m<sup>2</sup>K, and a constant heat transfer coefficient of 20 W/m<sup>2</sup>K was applied rest of the surfaces [57]. Table 3.2 shows the thermo-physical properties of base materials used in the calculation.

Table 3.2 Thermo-physical properties of aluminum alloy and steel sheets

Density, kg/m <sup>3</sup>	DP590	8000
	AA5052	2696
Solidus (T <sub>S</sub> ) and Liquidus (T <sub>L</sub> ) temperature, K	DP590	1673 and 1728 K
	AA5052	880 and 925 K
Specific heat, J/ kg K	DP590	448.11+3.7×10 <sup>-2</sup> T+1.61×10 <sup>-4</sup> T <sup>2</sup> -6.86×10 <sup>-8</sup> T <sup>3</sup>
	AA5052	929.0-0.627T+1.5×10 <sup>-3</sup> T <sup>2</sup> +4×10 <sup>-8</sup> T <sup>3</sup>
Thermal conductivity, W/ m K	DP590	3.79+3.85×10 <sup>-2</sup> T-4.18×10 <sup>-6</sup> T <sup>2</sup> -3.03×10 <sup>-9</sup> T <sup>3</sup>
	AA5052	25.2+0.398T+7×10 <sup>-6</sup> T <sup>2</sup> -3×10 <sup>-7</sup> T <sup>3</sup>
Yield Strength, MPa	DP590	356.58-0.29T-3.98×10 <sup>-5</sup> T <sup>2</sup> +5.55×10 <sup>-8</sup> T <sup>3</sup>
	AA5052	13.52+263.25×[1+exp{(T-456.5)/29}] <sup>-1</sup>



### 3.2.2 Analysis Method

#### (A) Heat Conduction Analysis

The spatial and temporal temperature distribution follows the un-stationary heat conduction governing equation. The governing equation [57,58] is as following

$$\rho c \frac{\partial T}{\partial t} = \lambda \left( \frac{\partial^2 T}{\partial x^2} + \frac{\partial^2 T}{\partial y^2} + \frac{\partial^2 T}{\partial z^2} \right) + \dot{Q} \quad (3.12)$$

where  $T$  is the temperature (K),  $\rho$  is the density ( $\text{g}/\text{m}^3$ ),  $\dot{Q}$  is the heat generation per volume ( $\text{W}/\text{m}^3$ ),  $t$  is the time (sec),  $\lambda$  is the thermal conductivity of isotropic material ( $\text{W}/\text{m}\cdot\text{K}$ ) and  $c$  is the specific heat ( $\text{J}/\text{kg}\cdot\text{K}$ ).

To solve the un-stationary heat conduction equation mentioned above, four boundary conditions are applied as following

1) When the temperature is determined on the boundary  $S_1$ :

$$T = \bar{T} \quad (3.13)$$

where  $\bar{T}$  is determined temperature.

2) When the heat flux ( $q_0$ ) flows from the boundary  $S_2$ :

$$q = q_0 \quad (3.14)$$

3) When heat transfer is on the boundary  $S_3$  for convection:

$$q = \alpha_c (T - T_c) \quad (3.15)$$

where  $\alpha_c$  is the convective heat transfer coefficient ( $\text{W}/\text{m}^2\cdot\text{K}$ ),  $T$  is boundary temperature of the object (K), and  $T_c$  is the outside temperature of the object (K).

4) When heat radiation is on the boundary  $S_4$ :

$$q = \sigma F(T^4 - T_r^4) \quad (3.16)$$

where  $\sigma$  is the Stefan Boltzmann constant,  $F$  is a compensation coefficient and  $T_r$  is the temperature of radiation source (K).

This equation can be changed into the form of linear equation for the ease of processing as following

$$q = \alpha_r(T - T_r) \quad (3.17)$$

$$\alpha_r = \sigma F(T + T_r)(T^2 - T_r^2) \quad (3.18)$$

Heat flux,  $q$  (W/m<sup>2</sup>), in normal to the boundary is derived from the Fourier's law as below:

$$q = -\lambda \frac{\partial T}{\partial n} \quad (3.19)$$

Galerkin's method is used to discretize the governing equation and corresponding boundary conditions. Internal temperature of the element  $T$  is given as following

$$T(x, y, z, t) = [N(x, y, z)]\{\emptyset(t)\} \quad (3.20)$$

where  $[N]$  is a shape function matrix shown the relation between nodal temperature and internal temperature of the element.  $\{\emptyset\}$  is the vector of the nodal temperature of the element at time  $(t)$ .

If Galerkin method is applied into equation (3.13) by using  $[N]$  as a weight function, the following equation (3.21) is obtained.

$$\int_{V^e} [N]^T \left\{ \lambda \left( \frac{\partial^2 T}{\partial x^2} + \frac{\partial^2 T}{\partial y^2} + \frac{\partial^2 T}{\partial z^2} \right) + \dot{Q} - \rho c \frac{\partial T}{\partial t} \right\} dV = 0 \quad (3.21)$$

where  $T$  shows transformation of matrix and  $V^e$  shows the domain of element. The second order term in partial differential equation (3.20) is alternated using Green-Gauss theorem as below,

$$\begin{aligned}
 & \int_{V^e} \lambda [N]^T \left( \frac{\partial^2 T}{\partial x^2} + \frac{\partial^2 T}{\partial y^2} + \frac{\partial^2 T}{\partial z^2} \right) dV \\
 &= - \int_{V^e} \lambda \left( \frac{\partial [N]^T}{\partial x} \frac{\partial T}{\partial x} + \frac{\partial [N]^T}{\partial y} \frac{\partial T}{\partial y} + \frac{\partial [N]^T}{\partial z} \frac{\partial T}{\partial z} \right) dV + \int_{S^e} \lambda [N]^T \left( \frac{\partial T}{\partial n} \right) dS
 \end{aligned} \tag{3.22}$$

where  $S^e$  is the boundary of element.

Equations (3.20) and (3.13) are substituted in equation (3.22), the right side of equation (3.22) becomes as follows:

$$- \int_{V^e} \lambda \left( \frac{\partial [N]^T}{\partial x} \frac{\partial [N]}{\partial x} + \frac{\partial [N]^T}{\partial y} \frac{\partial [N]}{\partial y} + \frac{\partial [N]^T}{\partial z} \frac{\partial [N]}{\partial z} \right) dV \cdot \{\phi(t)\} - \int_{S^e} q [N]^T dS \tag{3.23}$$

Using equation (3.22), equation (3.20) becomes finally as follows:

$$\begin{aligned}
 & - \int_{V^e} \lambda \left( \frac{\partial [N]^T}{\partial x} \frac{\partial [N]}{\partial x} + \frac{\partial [N]^T}{\partial y} \frac{\partial [N]}{\partial y} + \frac{\partial [N]^T}{\partial z} \frac{\partial [N]}{\partial z} \right) dV \cdot \{\phi(t)\} - \int_{S^e} q [N]^T dS + \int_{V^e} \dot{Q} [N]^T dV \\
 & - \int_{V^e} \rho c [N]^T [N] dV \cdot \frac{\partial \{\phi(t)\}}{\partial t} = 0
 \end{aligned} \tag{3.24}$$

Simplifying above equation (3.12), transient heat conduction problem can be expressed in finite element expression for an element as

$$[k] \{\phi\} + [c] \left\{ \frac{\partial \phi}{\partial t} \right\} = \{f\} \tag{3.25}$$

where  $[k]$ ,  $[c]$  and  $\{f\}$  show the heat conductivity matrix of an element, the heat capacity matrix of an element and the heat flow vector of an element, respectively. They are expressed as follows:

$$[k] = \int_{V^e} \lambda \left( \frac{\partial [N]^T}{\partial x} \frac{\partial [N]}{\partial x} + \frac{\partial [N]^T}{\partial y} \frac{\partial [N]}{\partial y} + \frac{\partial [N]^T}{\partial z} \frac{\partial [N]}{\partial z} \right) dV \tag{3.26}$$

$$[c] = \int_{V^e} \rho c [N]^T [N] dV \tag{3.27}$$

$$\{f\} = \int_{V^e} \dot{Q} [N]^T dV - \int_{S^e} q [N]^T dS \tag{3.28}$$

Boundary conditions at the boundary  $S_2$  to  $S_4$  [equation (3.14), (3.15) and (3.16)] are substituted in second term of equation (3.28).

When the heat flux,  $q_o$ , flows from the boundary  $S_2$ : the equation (3.14),

$$\int_{S_2^c} q[N]^T dS = \int_{S_2^c} q_o[N]^T dS \quad (3.29)$$

In the case of adiabatic boundary condition,  $q_o$  becomes zero (0).

When heat transfer is on the boundary  $S_3$  for convection: equation (3.15),

$$\int_{S_3^c} q[N]^T dS = \int_{S_3^c} \alpha_c(T - T_c)[N]^T dS \quad (3.30)$$

If  $T$  in the equation (3.30) is substituted by the equation (3.8), the equation (3.30) comes,

$$\int_{S_3^c} q[N]^T dS = \int_{S_3^c} \alpha_c[N]^T [N] dS \cdot \{\phi(t)\} - \int_{S_3^c} \alpha_c T_c [N]^T dS \quad (3.31)$$

When heat radiation is on the boundary  $S_4$ : equation (3.6),

$$\int_{S_4^c} q[N]^T dS = \int_{S_4^c} \alpha_r(T - T_r)[N]^T dS \quad (3.32)$$

If  $T$  in the equation (3.32) is substituted by the equation (3.8), the equation (3.32) forms below,

$$\int_{S_4^c} q[N]^T dS = \int_{S_4^c} \alpha_r[N]^T [N] dS \cdot \{\phi(t)\} - \int_{S_4^c} \alpha_r T_r [N]^T dS \quad (3.32)$$

From the above conditions, general boundary condition eliminated first boundary condition when the temperature is determined on the boundary  $S_1$  which can be applied to solve the transient heat conduction problem.

Equation (3.26) and (3.28) are modified using equation (3.29), (3.31) and (3.32) as below,

$$[k] = \int_{V^e} \lambda \left( \frac{\partial [N]^T}{\partial x} \frac{\partial [N]}{\partial x} + \frac{\partial [N]^T}{\partial y} \frac{\partial [N]}{\partial y} + \frac{\partial [N]^T}{\partial z} \frac{\partial [N]}{\partial z} \right) dV + \int_{S_3^e} \alpha_c [N]^T [N] dS + \int_{S_4^e} \alpha_r [N]^T [N] dS \quad (3.33)$$

$$\{f\} = \int_{V^e} \dot{Q} [N]^T dV - \int_{S_2^e} q_0 [N]^T dS + \int_{S_3^e} \alpha_c T_c [N]^T dS + \int_{S_4^e} \alpha_r T_r [N]^T dS \quad (3.34)$$

Therefore, finite element formula of an element can be derived as a form of matrix equation including boundary conditions by using equation (3.27), (3.33) and (3.34).

Finite element formula for the whole object analysed is constructed with assembled each matrix of elements and it can be expressed as following,

$$[K]\{\Phi\} + [C]\left\{\frac{\partial \Phi}{\partial t}\right\} = \{F\} \quad (3.35)$$

where  $\{\Phi\}$ ,  $[K]$ ,  $[C]$  and  $\{F\}$  show the nodal temperature vector, the heat conductivity matrix, the heat capacity matrix and the heat flow vector, respectively. They are given as below,

$$[\Phi] = \sum_e \phi, \quad [K] = \sum_e k, \quad [C] = \sum_e c, \quad \{F\} = \sum_e f \quad (3.36)$$

In this study, the numerical analysis for investigating the characteristics of thermal distribution of dissimilar welded joints (SPFC 590 DP/AA5052) by FSW and HFSW was proceeded based on the equation (3.35).

## (B) Thermal Elastic-plastic Analysis

The increment of strain in the element is given by differentiation of the internal displacements as below,

$$\{d\varepsilon\} = [B]\{dw\} \quad (3.37)$$

The increment of stress in element is obtained by using a matrix  $[D]$ , the elasticity matrix  $[D^e]$  or the plasticity matrix  $[D^p]$ .

$$d\sigma = [D]\{d\varepsilon\} \quad (3.38)$$

If the increment of initial strain  $\{d\varepsilon_0\}$  exists, stress increment is described as following,

$$\{d\sigma\} = [D]\{d\varepsilon - d\varepsilon_0\} \quad (3.39)$$

where the initial strains are function of temperature such as thermal strains and has a relation as following,

$$\{d\varepsilon_0\} = \{d\varepsilon^T\} = \{\alpha\}dT \quad (3.40)$$

Using equation (3.40), the increment of stress, equation (3.39), can be revised as following,

$$\{d\sigma\} = [D]\{d\varepsilon\} - [C]dT \quad (3.41)$$

Through the relationship between the nodal displacement which is  $\{dw\}$  and the increment of the nodal force which is  $\{dF\}$ , following equation (3.42) is obtained by applying the principle of virtual work.

$$\{dF\} = \int [B]^T [D] \{d\varepsilon\} dV - \int [B]^T [C] dT dV = [K] \{dW\} - \{dL\} \quad (3.42)$$

where,  $[K] = \int [B]^T [D] \{d\varepsilon\} dV$  is the stiffness matrix (3.43)

$$\{dL\} = \int [B]^T [C] dT dV \quad \text{is the nodal force due to initial strain} \quad (3.44)$$

The equilibrium of the whole object satisfying the additional equilibrium condition at each step of temperature increments can be constituted with individual equilibrium equation at individual nodes as below,

$$\sum \{dF\} = \sum [K] \{dW\} - \sum \{dL\} \quad (3.45)$$

When there is no external force acting at each node, equation (3.45) can be written in the simple form as following [1],

$$\sum \{dL\} = \sum [K] \{dw\} \quad (3.46)$$

### (C) Estimation of IMC Layer Thickness

Estimation for growth of the IMC layer considers parabolic law of diffusion in a cumulative manner throughout the interface temperature history [32,59]. The IMC layer thickness can be calculated based on the layer growth following the parabolic law of diffusion and its proportional characteristics of the square root of diffusion time as [33,59]

$$X = \sqrt{kt} = \sqrt{k_0 \exp\left(-\frac{q^*}{RT}\right)t} \quad (3.47)$$

where X represents the IMC layer growth;  $k_0$  is a exponential factor and  $q^*$  is the activation energy for the IMC layer growth. T is temperature and t is corresponding diffusion time, respectively.

Figure 3.3 depicts a typical transient temperature history at the joint interface that is utilized to exhibit the estimation of IMC layer thickness.

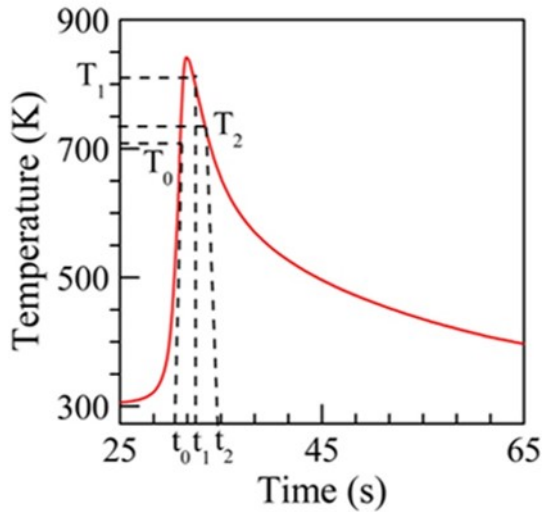


Figure 3.3 Prediction of the IMC layer thickness using temperature history at the joint interface



The growth of the IMC layer because of the time change from  $t_0$  to  $t_1$  and corresponding temperature change from  $T_0$  to  $T_1$  can be estimated as

$$X_1^2 = k_0 \exp \left[ -\frac{q^*}{R\{(T_0 + T_1)/2\}} \right] (t_1 - t_0) \quad (3.48)$$

where  $X_1$  was the estimated IMC layer thickness after time  $t_1$ . Likewise, the layer thickness  $X_2$  after time  $t_2$  is able to be estimated as

$$X_2^2 = X_1^2 + k_0 \exp \left[ -\frac{q^*}{R\{(T_1 + T_2)/2\}} \right] (t_2 - t_1) \quad (3.49)$$

or,

$$X_2 = \sqrt{X_1^2 + k_0 \exp \left[ -\frac{q^*}{R\{(T_1 + T_2)/2\}} \right] (t_2 - t_1)} \quad (3.50)$$

Thus, an overall function of estimation for the layer thickness with temperature history can be noted as,

$$X_{n+1} = \sqrt{X_n^2 + k_0 \exp \left[ -\frac{q^*}{R\{(T_{n+1} + T_n)/2\}} \right] (t_{n+1} - t_n)} \quad (3.51)$$

where  $X_{n+1}$  and  $X_n$  depicts the IMC layer thicknesses corresponding to temperature of interface as  $T_{n+1}$  and  $T_n$  with time of  $t_{n+1}$  and  $t_n$ . The values of  $k_0$ ,  $q^*$  and  $R$  are considered as  $1.32 \times 10^2 \text{ m}^2 \text{ s}^{-1}$ ,  $250 \text{ kJ mol}^{-1}$  and  $8.31 \text{ J mol}^{-1} \text{ K}^{-1}$ , respectively [59].

### 3.2.3 Numerical Model and Welding Condition

The shape and principal dimensions (600 mm (L) x 500 mm (W) x 2.5 mm (t of the aluminum alloy) and 1.4 mm (t of the steel)) of the models has been taken same as the experiment. The dimension of finite element model is shown in Figure 3.4, and applied welding conditions are shown in Table 3.3.

Numerical analysis is carried out on the butt welding of dissimilar materials as shown in Fig. 3.4. Assuming the heat flow is in unsteady state, 3 dimensional heat transfer model is adopted to conduct heat conduction and thermal elastic-plastic analysis for the dissimilar welded joints. 767550 numbers of nodes is adopted in the model, and the model is meshed into fine mesh from the interface to 20 mm away in both aluminum and steel side, but the other parts were applied as rough sized. The results are investigated and thermal and mechanical characteristics of dissimilar FSW and TIG assisted HFSW welded joints are demonstrated. From the result of heat conduction analysis, temperature history of the joint interface was measured to estimate the Fe-Al intermetallic compound (IMC ) layer thickness

Table 3.3 shows the welding conditions used in the study. The parameters were selected from preliminary trials. Similar rang of parameters were also reported in conventional FSW process which achieved continuous bead with maximum tensile strength more than 45% of the aluminum base metal [15].

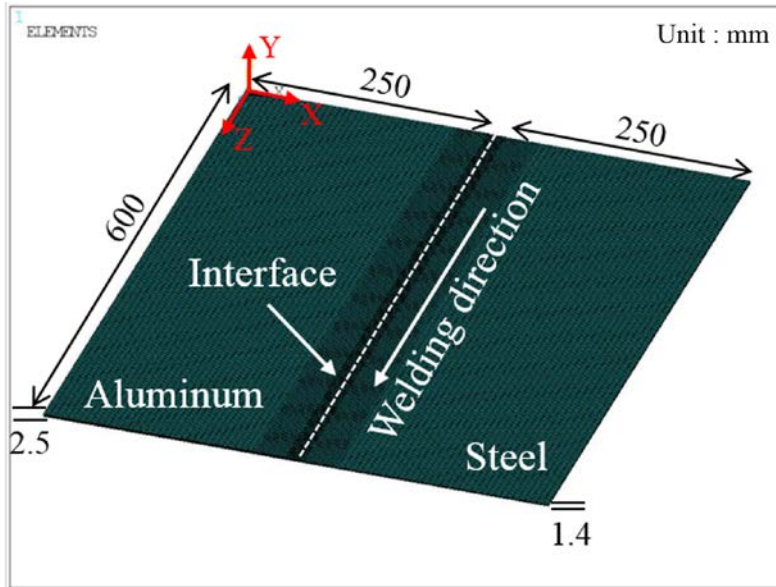


Figure 3.4 Configuration of numerical model for FSW and HFSW welded joints

Table 3.3 Welding conditions for dissimilar materials (Al502 to DP590)

Welding process	Moving speed (mm/sec)	RPM	Plunge Depth (mm)	Offset	TIG					
					Current (A)	Arc length (mm)	Distance to FSW tool (mm)	Distance to interface (mm)	Torch Inclination (°)	Shielding Gas (%)
FSW	1	400	2.3	Al:Fe = 9:1	-					
HFSW					20	2	20	5	60	Ar (99.99)
					30					
	40									

## 3.3 Thermal Characteristics

### 3.3.1 Temperature Distribution

Temperature distribution of dissimilar materials (Al5052-DP590) welded joints by friction stir welding (FSW) and TIG assisted hybrid friction stir welding (HFSW) is measured and compared to investigate the characteristics of heat conduction in the dissimilar materials welded joints. Figure 3.5 shows the numerically analyzed temperature distribution in FSW and HFSW of Al5052 aluminum alloy to DP590 steel sheets for different process conditions. Fig. 3.5 (a) shows a temperature distribution of FSW, and Fig. 3.5 (b) to Fig. 3.5 (d) plot the temperature distribution in HFSW with TIG current as 20, 30, and 40 A, respectively. In the process of HFSW, which is shown in Fig. 3.5 (b) to (d), the front and rear contour of temperature above 600 K indicates temperature distribution due to TIG preheat source and FSW tool. In Fig. 3.5 (a), the maximum temperature appears in the steel side as 754.64 K and wider temperature distribution is observed in the aluminum alloy side. From Fig 3.5 (b) to Fig. 3.5 (d), the maximum temperature appears in the steel side as 786.6 K, 813.37 K, and 842.42 K, respectively. The wider temperature distribution in the aluminum side than in the steel side is because higher thermal conductivity of the aluminum alloy allows to the heat to be conducted faster in the aluminum alloy. Plus, the generation of maximum temperature in the steel side can be attributed to the difference of thermo-physical properties between the aluminum alloy and the steel, such as higher coefficient of friction of the steel than that of the aluminum alloy. Figure 3.5 depicts temperature distribution in the aluminum alloy surface is below the aluminum liquids temperature, while steel surface experiences maximum temperature below the liquidus temperature of steel (1773 K). It can presume that pre-heating of steel surface below its melting temperature by TIG arc softens the harder material and improves the plastic flow of the material.

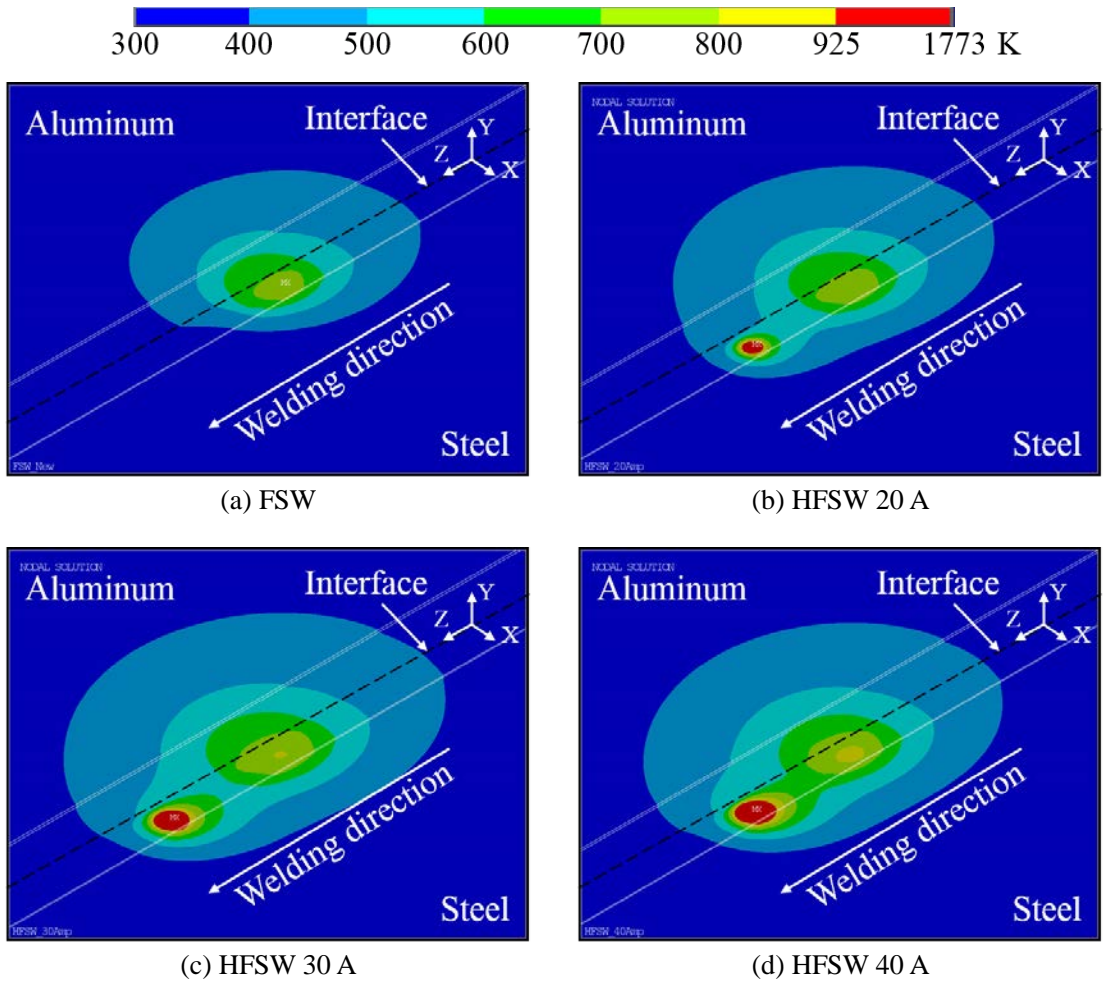


Figure 3.5 Temperature distribution in FSW and HFSW welded joints with welding current of 20, 30, and 40 A

Figure 3.6 shows sectional view of temperature distribution in aluminum alloy side along the joint interface. It can be seen that the widths of temperature region are maximum at the top surface and reduce towards the thickness direction that can be attributed to the higher amount of heat generation due to friction at the tool shoulder to workpiece interface than pin to workpiece interface. Additionally, the maximum temperature contour in aluminum side is 0.7 – 0.8 times (700 – 800 K) of aluminum liquidus temperature (925 K), which can be considered as a stir region.

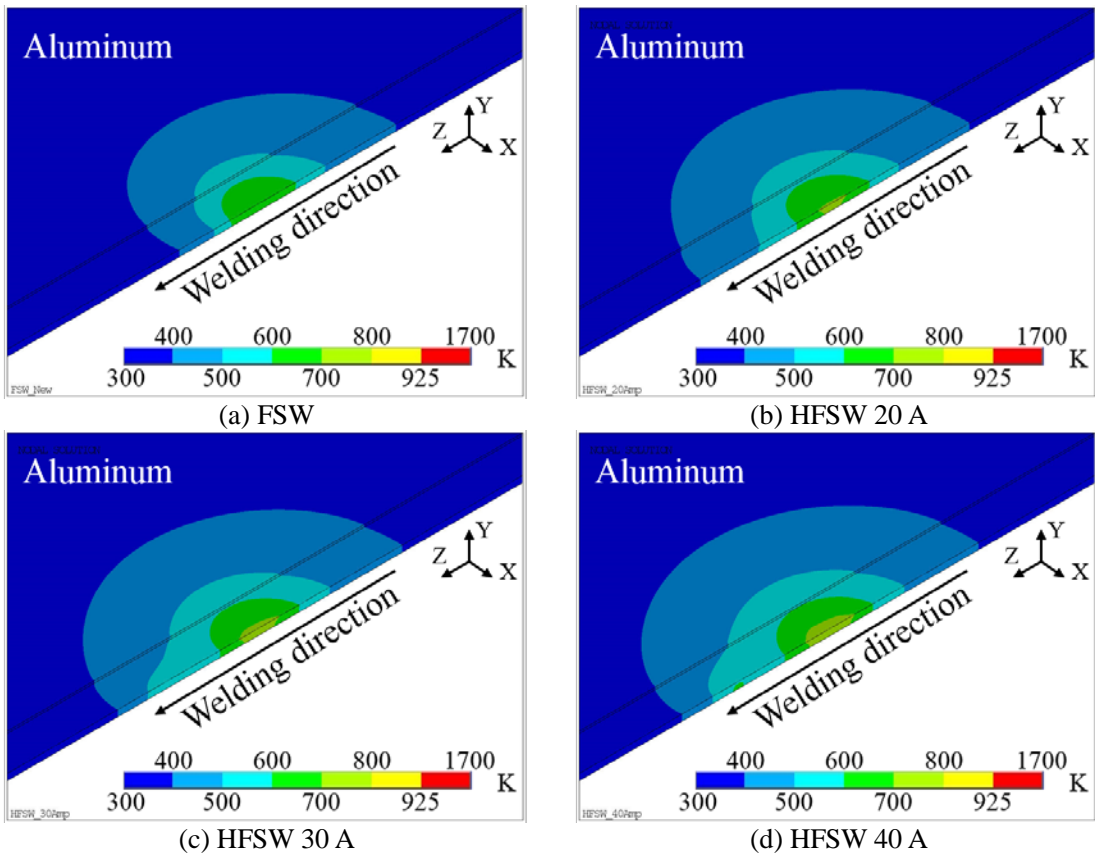
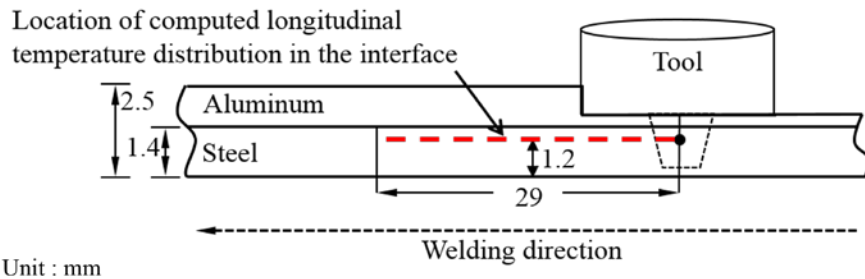
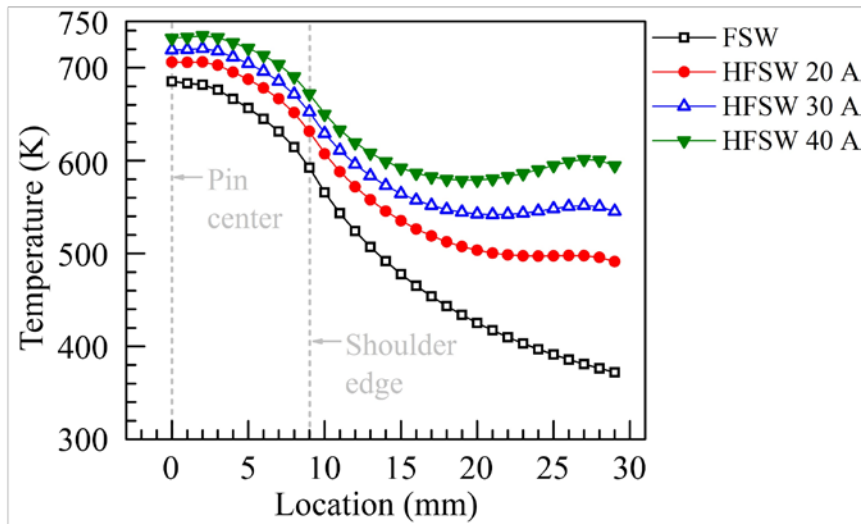


Figure 3.6 Sectional view of temperature distribution in Al side along the joint interface

Figure 3.7 shows a comparison of the longitudinal temperature distribution of the interface 1.2 mm above from the bottom surface and between the location which is vertical to the TIG center and which is also vertical to the pin center with the condition of conventional FSW and HFSW with TIG current 20, 30, 40 A. Fig. 3.7 (a) depicts the location of measured the longitudinal temperature distribution estimated by numerical analysis, and Fig. 3.7 (b) shows the longitudinal temperature distribution profile in the interface by FSW and HFSW process, respectively. The maximum temperature of conventional FSW process is observed as 686.48 K, and the maximum temperature of the HFSW process is observed as 706.32, 720.77, and 734.71 K when the TIG current was applied as 20, 30, and 40 A respectively. The locations of the maximum temperature appeared are near the pin-workpiece interface in all conditions because there is the highest rate of heat generation from the plastic deformation through pin-workpiece interface and the friction and plastic deformation through tool shoulder-workpiece interface . The preheating source, TIG, also induces the FSW tool to rotate in the environment of temperature increased material which leads increased plastic flow in 519.02, 559.78, and 607.40 K when the TIG current was 20, 30, and 40 A, respectively.



(a) Schematics of longitudinal temperature distribution measurement



(b) Longitudinal temperature profile of the interface

Figure 3.7 Longitudinal temperature distribution of the interface from the tool center to TIG in FSW and HFSW welded joints



Figure 3.9 shows the numerically analyzed temperature variations along the transverse direction to the weld line which is measured 0.9 mm above from the bottom surface in Figure 3.8, during welding. The maximum temperature appears as 754.60, 1153.2, 1492.2, and 1648.7 K in the condition of conventional FSW, HFSW with TIG current 20, 30, and 40 A, respectively. The peak temperature in FSW is observed in the steel side, especially in the region attached or close to the tool pin, and all HFSW process show their peak temperature in the center of arc from TIG, respectively. However, the peak temperature appeared by the tool in all condition is observed in the steel side, especially in the region near from to the tool pin as 754.60, 785.6, 811.23, and 841.92 K, respectively. Higher peak temperature occurred in the steel side than in the aluminum side due to the lower heat conductivity of the steel and the friction between the pin to DP590 inducing higher heat generation rate during the process, despite the location of the pin is biased into the aluminum side. Compared to the steel side, the aluminum alloy side achieved swift heat conduction at the same distance from the center of the model and it also shows higher cooling rate. Heat is conducted rapidly toward the aluminum alloy elements, and thus, temperature is raised throughout the aluminum alloy within a very short time compared to DP590 side. This is mainly because of higher value of heat conductivity of the aluminum alloy.

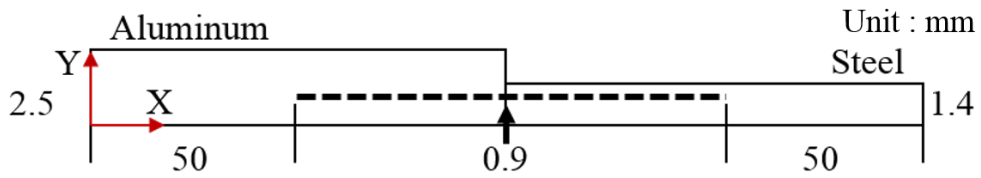


Figure 3.8 Schematics of location for the measurement of the temperature variation along the width direction

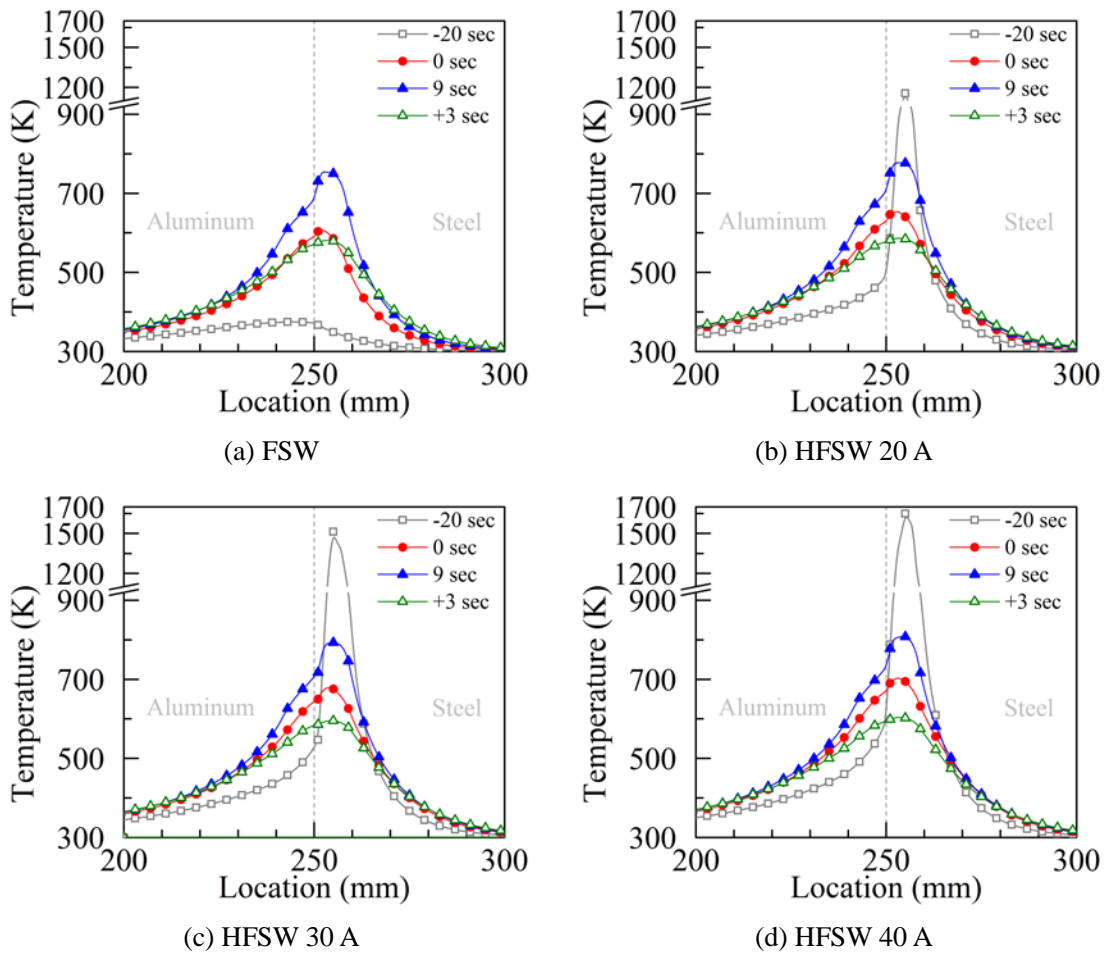


Figure 3.9 Temperature variation along the width direction in FSW and HFSW welded joints with time

Figure 3.11 shows a comparison between numerically analyzed the experimentally measured thermal histories the thermocouple monitoring locations shown in Figure 3.10 for different process conditions and at a constant moving speed of 1 mm/sec and rotational speed of 400 rpm. As shown in Fig. 3.10, the temperature history is measured at a depth of 0.9 mm from the bottom surface and 16 mm away from the interface. Fig. 3.11 (a) and (b) show the temperature histories respectively in the aluminum and the steel side of FSW process (TIG current 0A). The numerical (drawn as blue dotted line) and measured values (drawn as red solid line) of peak temperatures are 512 and 515 K in aluminum side (Fig. 3.11 a), and 439 and 407 K in steel side (Fig. 3.11 b), respectively. Besides, Fig. 3.11 (c) and (d) show temperature histories in aluminum and steel side for HFSW with welding current of 20 A, and Fig. 3.11 (e), (f) and Fig. 3.11 (g), (h) show the same for TIG current of 30 and 40 A, respectively. The values of numerically analyzed (marked by dotted line) and measured (marked by solid line) peak temperatures are 552.5 and 551.5 K in Fig. 3.11 (c), 460 and 457 K in Fig. 3.11 (d), 563.7 and 563.4 K in Fig. 3.11 (e) and 473.6 and 471 K in Fig. 3.11 (f), respectively. The existence of two crests in the temperature histories could be noted in Fig. 3.11 (d), (f), and (h). The first crest represents an increase in temperature at the thermocouple monitoring location due to the TIG preheat source, while second crest depicts change of temperature at the same location by the FSW tool.

A comparison of Fig. 3.11 (a), (c), (e), (g) and of (b), (d), (f), (h) shows the values of peak temperatures in both aluminum alloy and steel side are lower in conventional FSW process than that of the HFSW process. That can be attributed to an increase in heat generation per unit length of the joint by external TIG preheat heat source in HFSW process. Fig. 3.11 (c) and (e), (d) and (f), and (g) and (h) depict peak temperatures in both aluminum and steel side increase with rise in TIG welding current from 20 to 40 A in HFSW process, that can be attribute to the higher heat generation at high welding current. A fair agreement between the numerically computed and corresponding experimentally measured temperature history has been observed in Fig. 3.11. A fair agree between the numerical computations and the experimental result is confirmed, and the thermal histories of them represent a quick rise to the peak temperature followed by comparatively sluggish cooling that can be attributed to the faster rate of heat generation as the tool approaches and slower rate of cooling as the tool passes the checked location.

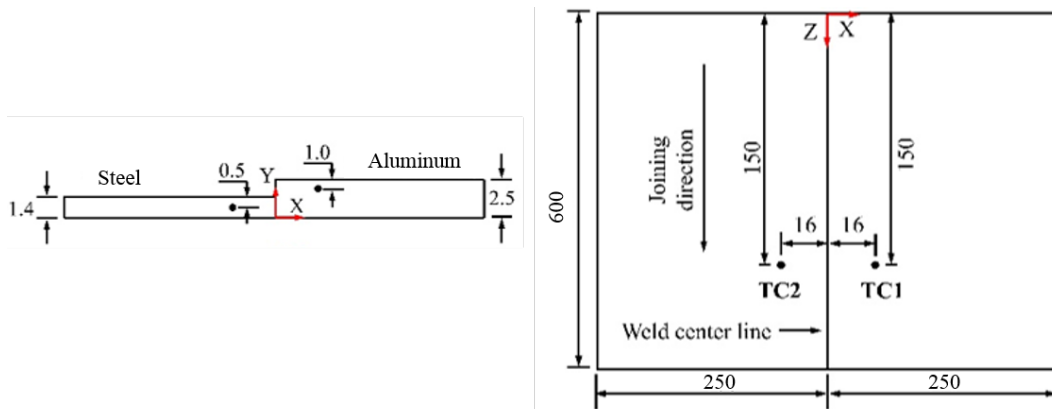


Figure 3.10 Schematics of locations for the measurement of temperature history

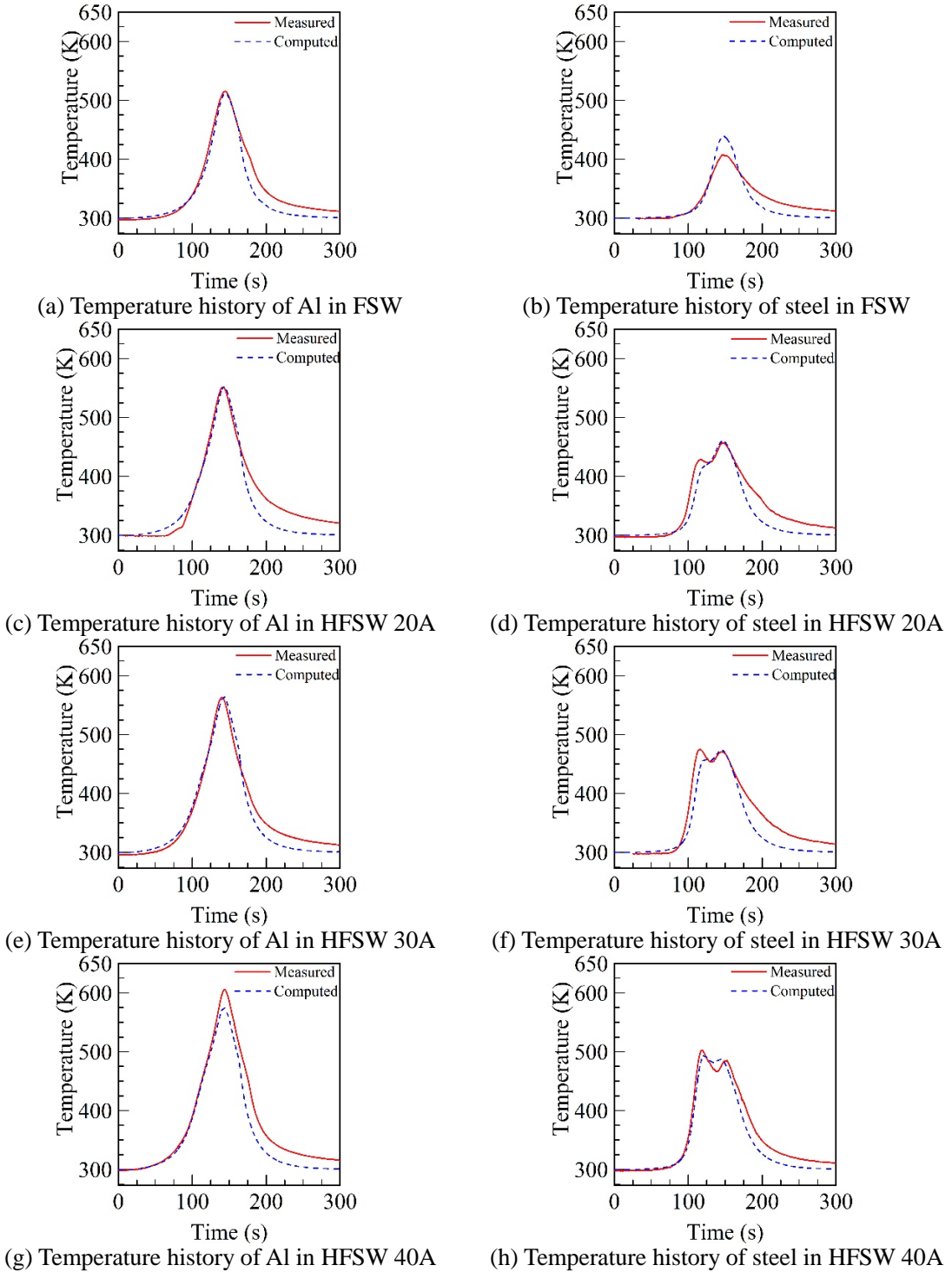


Figure 3.11 Temperature history of FSW and HFSW process

### 3.3.2 Fe-Al Intermetallic Compound Layer Thickness

The numerical results are used to estimate the temperature history at the joint interface. Figure 3.12 shows the schematics of checked locations for estimating intermetallic compound (IMC) layer thickness, and following Figure 3.13 shows the numerical result of the temperature history at the interface of dissimilar Al5052-DP590 joints from conventional FSW and HFSW with TIG current as 20, 30, and 40 A, respectively. The IMC layer thickness is measured at 1.2 mm from the bottom surface of the interface along the thickness. Fig. 3.13 (a) shows the computed interface temperature history for conventional FSW, and Fig. 3.13 (b) to (d) illustrate HFSW with TIG current of 20, 30, and 40 A, respectively. The maximum numerically analyzed peak temperature in each condition in the sequence mentioned above was 686.48, 706.32, 720.77, and 734.71 K, respectively. In Fig. 3.13 (b) to (d), furthermore, a small bulge can be seen in the heating period of temperature history that can be attributed to the change of temperature due to preheated TIG source. The numerically computed temperature history of the joint interface in each condition which is shown in Fig. 3.13 was used to estimate the thickness of IMC layer in the joint interface by substituting into the equation (3.51).

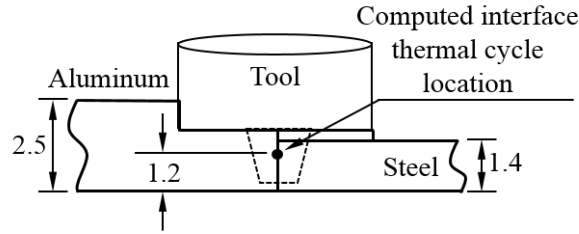


Figure 3.12 Schematics of location for the measurement of temperature history in the interface

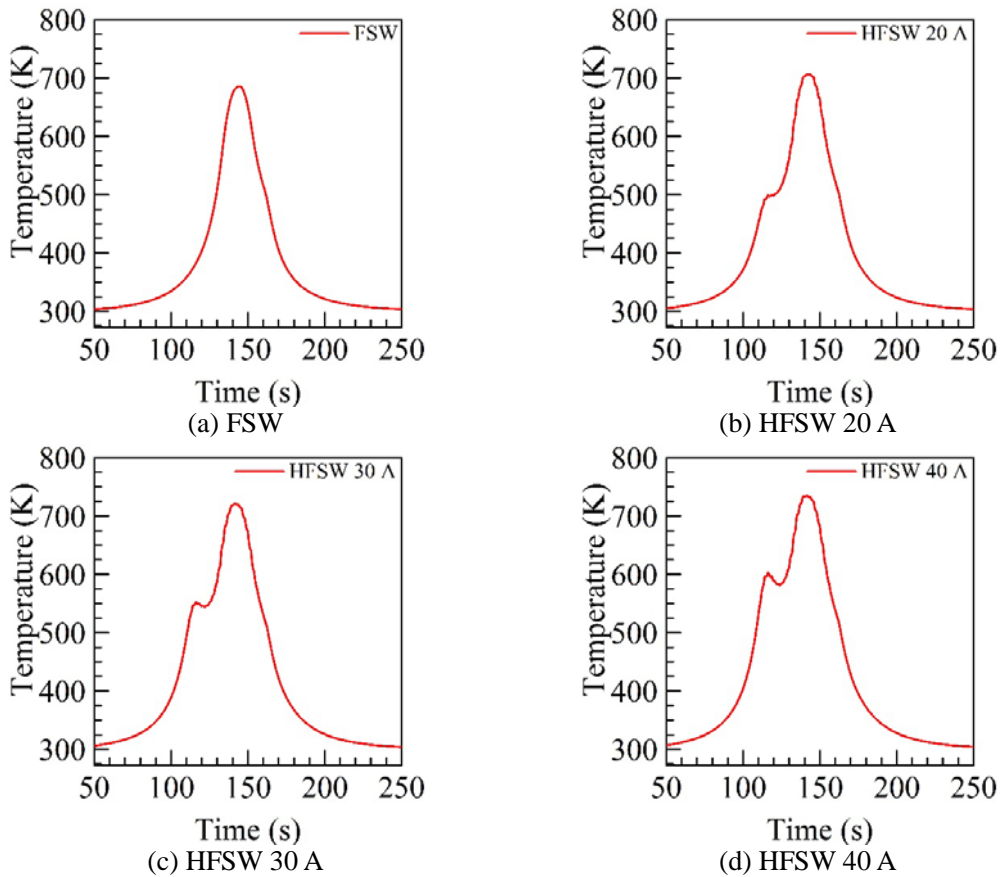


Figure 3.13 Temperature history of the interface in FSW and HFSW welded joints

In Figure 3.14, the maximum temperature at the interface increases from 686.48 to 734.71 K with an increase in TIG current from 0 to 40 A. In another words, it can be inferred that there is the surge in heat generation per unit length of the welded joints at higher welding current. In Table 3.4, the estimated IMC layer thickness is illustrated. The formation of IMC layer thickness is estimated as 1.39  $\mu\text{m}$  in conventional FSW process, 2.29, 3.72, and 5.44  $\mu\text{m}$  in HFSW process with TIG current as 20, 30, and 40 A, respectively. As comparison of each condition, the value of estimated IMC thickness tended to be decreased as the material experiences less heat variation. The Fe-Al IMC layer, which is brittle and decreases the joint strength but is unavoidable to weld the dissimilar materials, remained within a range under 10  $\mu\text{m}$ .

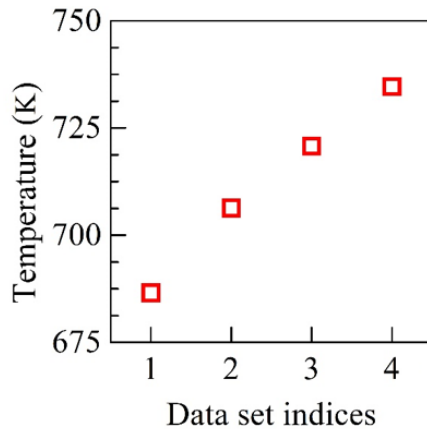


Fig. 3.14 The maximum temperature at the interface in FSW and HFSW welded joints

Table 3.4 Estimated IMC layer thickness at the interface

Welding process	Maximum temperature (K)	Estimated IMC layer thickness ( $\mu\text{m}$ )
FSW (Indices 1)	686.48	1.39
HFSW 20 A (Indices 2)	706.32	2.29
HFSW 30 A (Indices 3)	720.77	3.72
HFSW 40 A (Indices 4)	734.71	5.44



Figure 3.15 shows the SEM macrographs of Fe-Al intermetallic compound layer at different welding conditions of FSW and HFSW processes. The steel is located at the left side, while the aluminum alloy is at the right side. The thickness of the IMC layers were measured at several locations along the joint interface and average value was considered. In Fig. 3.15 (a) showing the IMC layer formation in conventional process, the average value of IMC layer with standard deviation was  $2.04 (\pm 0.222) \mu\text{m}$ . In Fig. 3.15 (b) to (d), IMC layer thickness in HFSW with TIG current 20, 30, and 40 A depict the average values as  $2.77 (\pm 0.316)$ ,  $3.18 (\pm 0.5)$ , and  $3.94 (\pm 0.518) \mu\text{m}$ , respectively. The increase of IMC layer can be attributed to the higher amount of heat generation at high TIG pre-heat source current. The morphology of the IMC layer was serrated type and oriented towards the aluminum alloy side that implied non-uniform diffusion between Fe and Al at the interface.

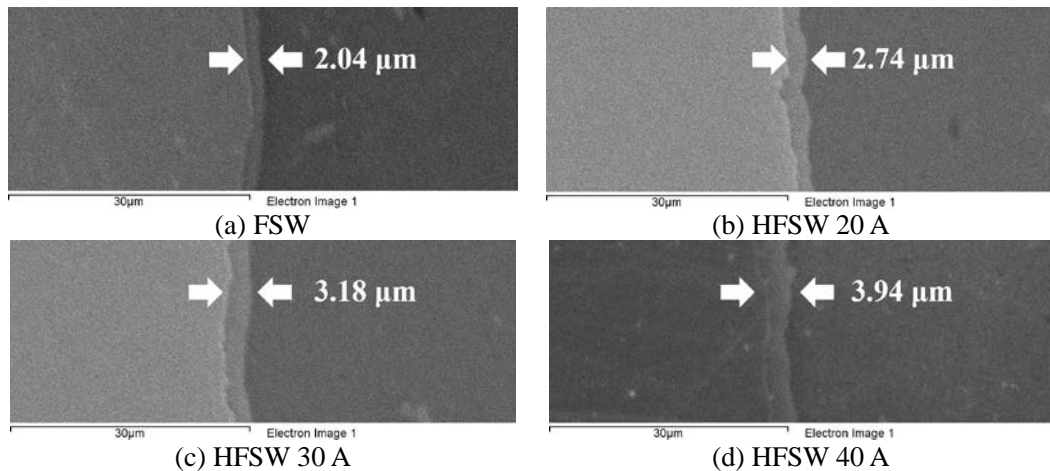


Figure 3.15 SEM images of IMC layer in FSW and HFSW process

Table 3.5 and Figure 3.16 show the comparison of numerically estimated and experimentally measured IMC layer thickness for different joining conditions. Data set index 1 presents the thickness of layer in conventional FSW, and indices 2 to 4 show layer thickness for HFSW process with TIG current of 20 to 40 A. Fig. 3.16 illustrates an increase in TIG current from 0 to 40 A increases numerically computed (marked by blue circle) IMC layer thickness from 1.4 to 5.4  $\mu\text{m}$ , and corresponding experimentally measured (marked by red square) thickness varies from 2.04 ( $\pm 0.222$ ) to 3.94 ( $\pm 0.518$ )  $\mu\text{m}$ . The numerically analyzed IMC layer thickness at the joint interface are found to be reasonably fair in comparison to the corresponding measured results. Furthermore, formed IMC layer thickness in each condition satisfied under 10  $\mu\text{m}$  thickness. [23,60]

Table 3.5 Comparison of IMC layer thickness between numerical and experimental results

Welding process	IMC Layer Thickness ( $\mu\text{m}$ )	
	Computed	Measured
FSW (Indices 1)	1.39	2.04
HFSW 20 A (Indices 2)	2.29	2.77
HFSW 30 A (Indices 3)	3.72	3.18
HFSW 40 A (Indices 4)	5.44	3.94

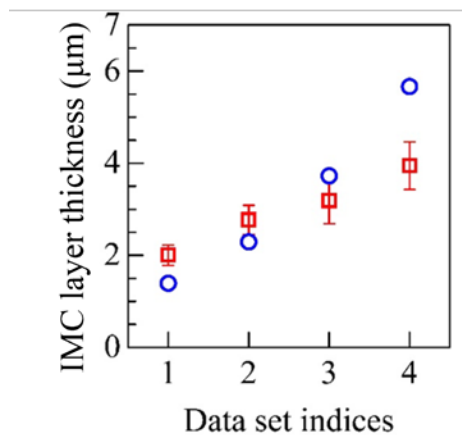


Figure 3.16 Comparison of IMC later thickness between experimental and numerical results

## 3.4 Mechanical Characteristics

### 3.4.1 Residual Stress

Figure 3.17 shows the transient stress generated in dissimilar materials FSW and HFSW 20 A welded joints perpendicular to the weld line. Fig. 3.17 (a) and (b) depict the longitudinal residual stress profile at 0 second which is the starting of the welding of FSW and HFSW, respectively. Fig. 3.17 (c), (d) show the profiles at 9 second during welding, and Fig.3.17 (e), (f), and (g), (h) depict the profile of during cooling which is at 12 second, and after cooling which is at 1172 second, respectively. The longitudinal residual stress profiles ( $\sigma_{zz}$ ) is measured at the distance of 1.2 mm over bottom surface ( $y=1.2$  mm) of the dissimilar materials welded joints. In Fig. 3.17 (a) to (d), when heat is input to the center of the model, compressive stress is generated immediately in both aluminum alloy and steel sides. Compared to FSW which shows maximum longitudinal stress as 75 MPa in the steel side during welding, HFSW shows 18 % higher value of transient stress in the steel side as 89 MPa due to increased thermal load by preheating effect of TIG. In Fig. 3.17 (g) and (h), consequently, it is also observed that HFSW generates slightly higher longitudinal residual stress ( $\sigma_{zz}$ ) as 296.2 MPa than FSW which shows its residual stress as 273.7 MPa due to increased thermal load by TIG.

It has been previously observed that the longitudinal residual stress occurred in FSW of similar materials shows “M-Like” profile [61,62], and is lower relative to the yield strength of base metal [63,64]. However, the occurred stress profiles of the dissimilar welded joints toward perpendicular direction to the weld line in this study follows asymmetric ‘M-like’ shape in Fig. 3.17 because of the different thermal expansion coefficients between the aluminum alloy and the steel which has the lower value than the aluminum has. During cooling of dissimilar materials welded joints, the aluminum side which has larger thermal expansion coefficient shrinks more than the steel does, and this acts as an internal constraint force on the steel. Additionally, the residual stress distribution by FSW process is recognized as a combination of two single-peaked profiles of tensile residual stress at the edges of the tool shoulder [65]. This is because the heat input during welding is assumed to be generated by the friction between the tool shoulder and the surface of workpiece, so the heat generation is no longer focused on a narrow weld line but applied on a broad region that is the same width of the shoulder diameter. The strongest temperature gradients are expected to be at the edges of the shoulder, and this area is characterized by the highest tangential speeds of the tool and the highest heat generation rate. In other words, the last region cooled down is the distance from the weld center to the edge of the shoulder.

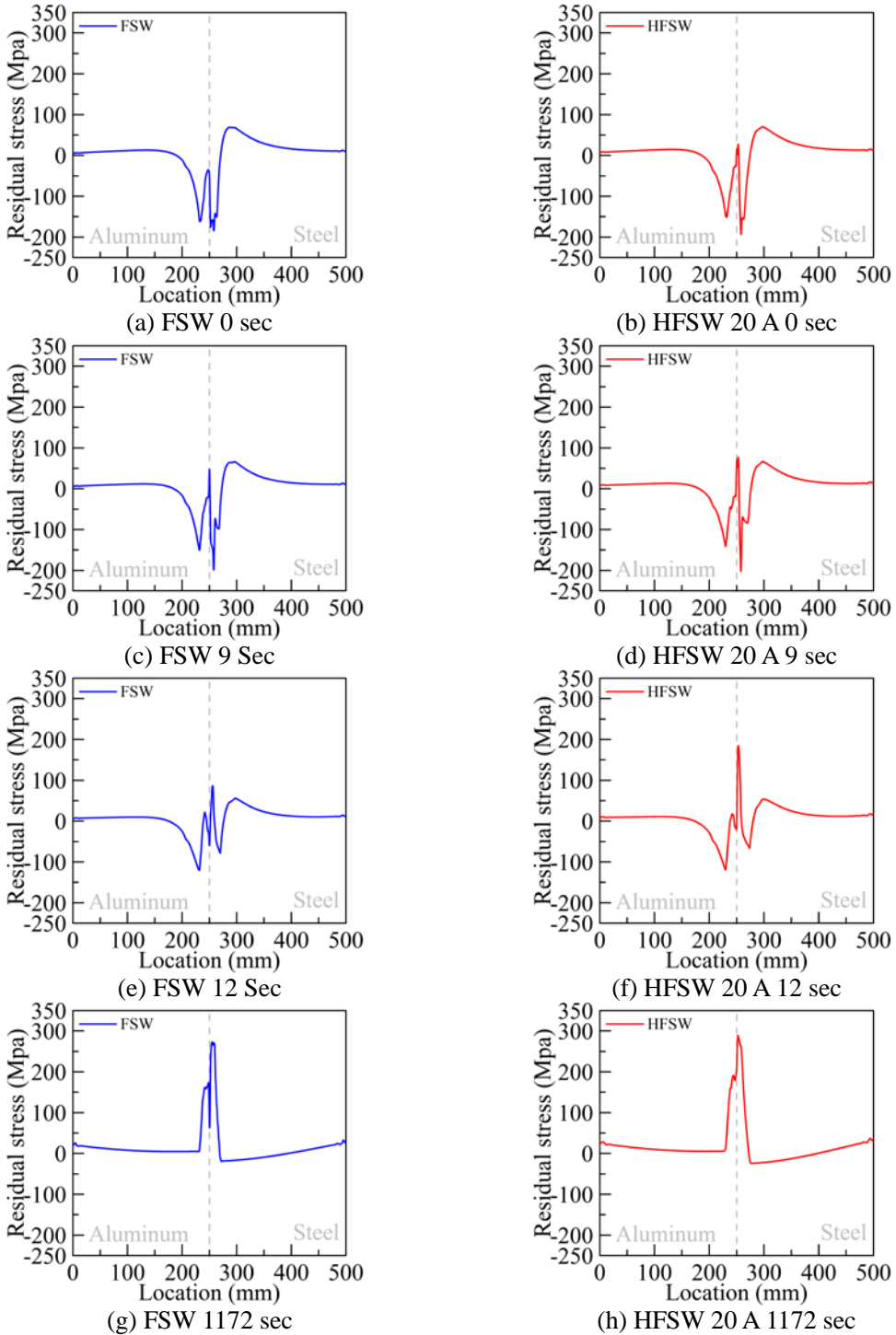
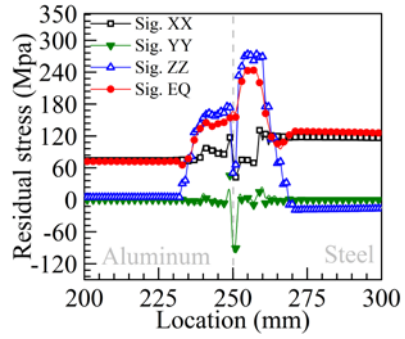
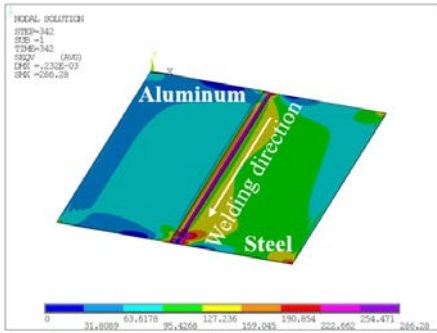
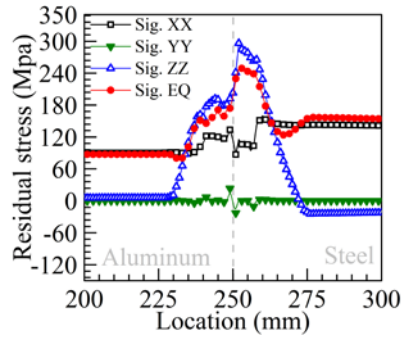
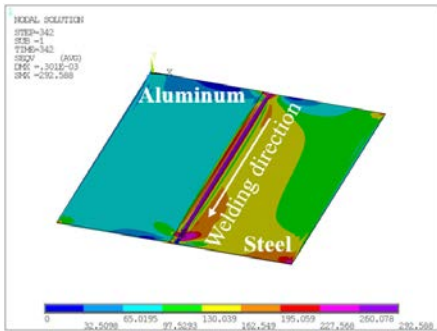


Figure 3.17 Distribution of transient welding stress  $\sigma_{zz}$  in FSW and HFSW welded joints

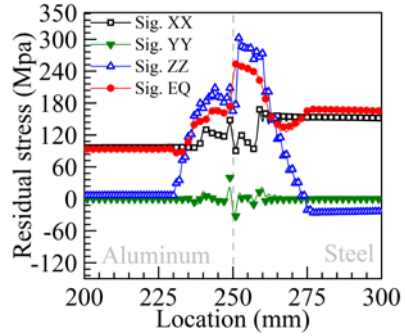
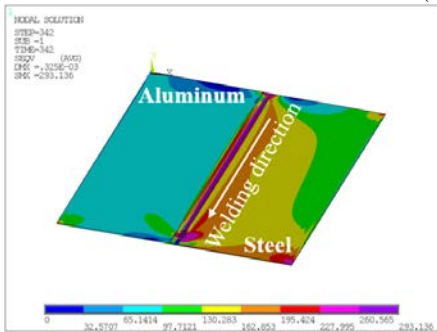
Figure 3.18 plots the distribution of equivalent residual stress of the dissimilar materials (Al5052/DP590) welded joints in FSW and HFSW process on the left side, and the residual stress profiles ( $\sigma_{XX}$ ,  $\sigma_{YY}$ ,  $\sigma_{ZZ}$ ,  $\sigma_{EQ}$ ) along the width direction at distance of 1.2 mm over bottom surface ( $y=1.2$  mm) of the dissimilar materials welded joints in the right side, respectively. The residual stress distribution of aluminum alloy and steel were asymmetric. Noting the longitudinal residual stress ( $\sigma_{zz}$ ) is higher in the steel side of welded joints than in the aluminum alloy side, the maximum tensile residual stress level of DP590 side of FSW welded joints is about 273.7 Mpa which is 60 % of the yield strength of the steel (459 MPa). Compared to the maximum longitudinal residual stress ( $\sigma_{zz}$ ) of the conventional FSW welded joints, residual stress ( $\sigma_{zz}$ ) formed by HFSW depicted in Fig. 3.18 (b), (c), and (d) show slightly higher value due to the higher heat input by the preheating source. In sequence, the maximum value of the longitudinal residual stress ( $\sigma_{zz}$ ) of HFSW 20, 30, and 40 A is shown as 296.2, 307.4, 321.0 MPa, respectively. In another words, HFSW 20, 30, 40 A process show 5, 7, 10 % higher residual stress ( $\sigma_{zz}$ ), respectively. Furthermore, residual stress around the weld line shows a sudden change due to the differences in the cooling rate and material properties of the aluminum alloy and the steel. Especially, thermal expansion coefficient of the aluminum alloy is larger than that of the steel, thus the aluminum leads larger shrinkage than the steel does during cooling. Therefore, the larger shrinkage of the aluminum side acts as a constraint force to the steel, and induces the generation of higher residual stress in the steel side. It can be also confirmed that the higher value of the residual stress ( $\sigma_{zz}$ ) around the weld line by HFSW than that by FSW is due to the higher heat input by preheating source TIG applied increased thermal load. For the total equivalent residual stress, preheating source increased the thermal load into the specimens, and thus the residual stress of the HFSW 20 A welded joints increased 2 % as 292 MPa than the conventional FSW (286 MPa). Moreover, the tensile residual stress level of the steel side of welded joints is escalated drastically than the tensile residual stress level in FSW welded joints because shrinkage of the aluminum alloy acted as constraint force more actively.



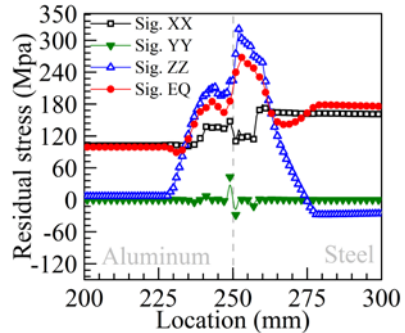
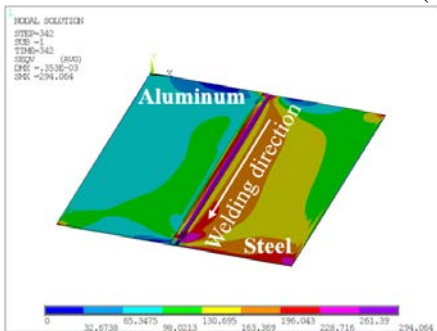
(a) FSW



(c) HFSW 20 A



(e) HFSW 30 A



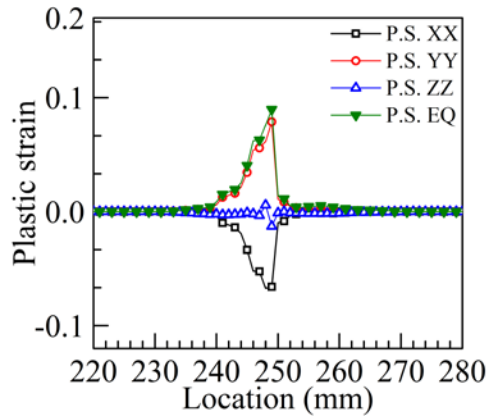
(g) HFSW 40 A

Fig. 3.18 Distribution of welding residual stress in FSW and HFSW welded joints

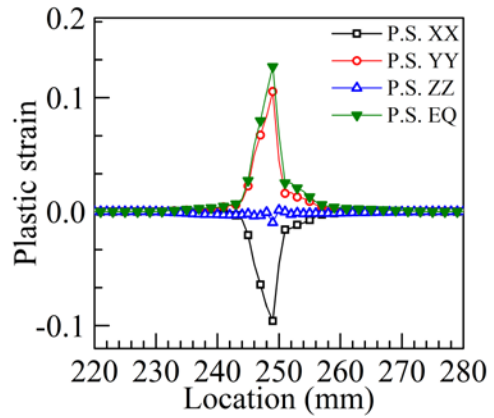
### 3.4.2 Plastic Strain

Figure 3.19 shows the distribution of plastic strain profiles along the width direction in FSW and HFSW welded joints after cooling down to the room temperature (300 K). The measured location for Fig. 3.19 is 1.2 mm over the bottom surface ( $y=1.2$  mm) of dissimilar materials welded joints. Fig. 3.19 (a) shows the plastic strain of workpiece in the FSW process, and (b), (c), (d) illustrate the plastic strain of the workpiece in HFSW with TIG current as 20, 30, 40 A, respectively. It is found that the range of plastic strain is widely spread in the aluminum alloy side than in the steel side, and it may be because of the wider area of heat input from the offset of the FSW tool. In terms of the FSW process, the maximum equivalent plastic strain is observed in the aluminum side as 0.090185 at 1 mm away from the interface due to the highest heat input. The maximum equivalent plastic strain in the welded joints over all conditions is following as  $\varepsilon_{EQ}^P(HFSW\ 40\ A)(= 0.157) > \varepsilon_{EQ}^P(HFSW\ 30\ A)(= 0.134) > \varepsilon_{EQ}^P(HFSW\ 20\ A)(= 0.125) > \varepsilon_{EQ}^P(FSW)(= 0.090)$ . The maximum plastic strain of HFSW 20 A is slightly higher as 0.035 than that of FSW. It is confirmed that the maximum plastic strain was occurred in the aluminum alloy side, and the order is following the order of the applied thermal load from the maximum to the minimum amount.

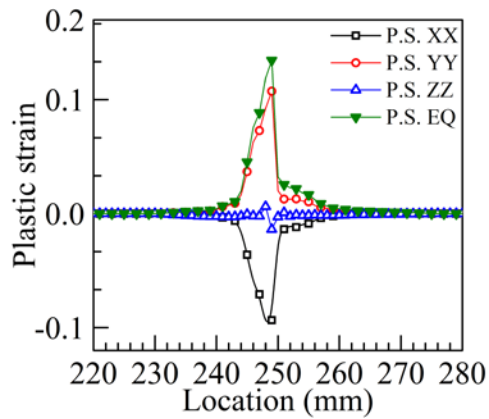




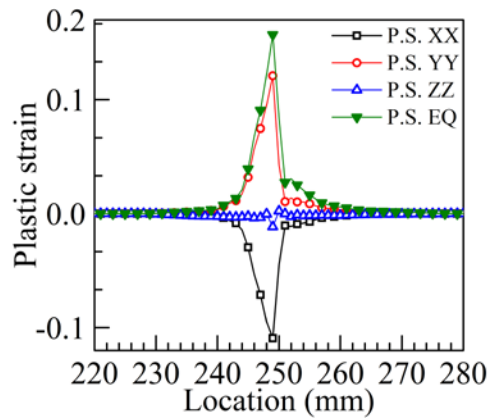
(a) FSW



(b) HFSW 20 A



(c) HFSW 30 A



(d) HFSW 40 A

Fig. 3.19 Distribution of plastic strain in FSW and HFSW welded joints

### 3.5 Conclusion

In present study, welding temperature field with temperature history, estimation of intermetallic compound (IMC) layer thickness, residual stress field, and plastic strain field in dissimilar materials welded joints of Al5052 (aluminum alloy) and DP590 (high-strength steel) has been investigated by numerical simulation and compared with experimental result. The numerical results show fair agreements with the experimental results. The results can be summarized as follow:

- An asymmetric heat conduction phenomenon is observed in the dissimilar materials (Al5052-DP590) welded joints. The temperature gradient in steel plate was stiffer than that in aluminum alloy because the thermal conductivity of the aluminum was much higher than that of the steel. In other words, the temperature field of the aluminum shows wider region than that of the steel shows.
- To validate the result of numerical analysis, comparison of the temperature history between numerical result and experimental result measured by thermocouple is carried out. As a result, the numerical result of the temperature history was fairly matched with experimentally measured temperature history. The result of the comparison indicates the adopted numerical model is proper to simulate the estimation of IMC layer thickness.
- The estimated IMC layer thickness in each welding condition by using the temperature history of the joint interface was compared with experimentally measured and showed fair agreement. Compared to the IMC layer of FSW, HFSW 20 A process formed slightly thicker layer. The increase of IMC layer can be attributed to the higher amount of heat generation at high TIG pre-heat source current. The numerically analyzed IMC layer thickness at the joint interface are found to be

reasonably fair in comparison to the corresponding measured results. Moreover, the thickness IMC layer satisfied under 10  $\mu\text{m}$  thickness.

- The peak value of longitudinal stress ( $\sigma_{zz}$ ) was generated in the high strength steel side as 296.2 MPa in HFSW 20 A condition, which is 5 % higher than that in FSW (273.7 MPa). Moreover, the plastic strain of HFSW 20 A generated was 0.035 higher than that of FSW generated.

## Chapter 4

### Summary

In this paper, the thermal and mechanical characteristics of conventional Friction Stir Welding (FSW) and TIG assisted hybrid Friction Stir Welding (HFSW) on dissimilar materials (aluminum alloy and high strength steel) are studied through the numerical analysis and compared with experimental result to obtain reliability dissimilar materials welded joints. Feasibility to join 2.5 mm thick aluminum alloy (Al5052) and 1.4 mm thick high strength steel (DP590) by conventional FSW process (FSW) and TIG-assisted HFSW process (HFSW) is studied through experimental and numerical analysis. In numerical simulation, both of welding systems were proceed with heat conduction analysis and elastic-plastic analysis. Moreover, the characteristics of mechanical and metallurgical of dissimilar materials welded joints obtained by conventional FSW and HFSW are investigated.

Recently, joining light materials gets focus in automotive industry because weight reduction of vehicle with light materials can be a good solution to improve fuel efficiency for corresponding the reinforced emission gas regulations. However, adopting aluminum alloy and high strength steel which are lighter than conventional steels have been used in the industry is challenging when they are joined with conventional fusion welding process. Notably, not only their difference of chemical properties which leads forming brittle IMC layer but also their big gap of thermo-physical properties, such as coefficient of thermal expansion and thermal conductivity, are the main factors to overcome to join. Especially, the intermetallic compounds layer formation has to be below than 10  $\mu\text{m}$  thickness because a thick intermetallic compounds layer would cause the brittleness of the welded joints and be easier to experience crack initiation and propagation [23,60].

The problem mentioned above can be avoided by employing a solid-state welding such as

FSW, but lack of plastic flow and excessive tool wear lead significant limitations to this process. The HFSW can overcome the problems by adding an additional heat source in front of the FSW tool to pre-heat the material which has higher melting temperature resulting in improvement of plastic flow and in reduction of the plunging force to the tool during welding.

In Chapter I, research background, objectives, and construction of the thesis are described.

In Chapter II, experimental researches based on conventional friction stir welding and TIG assisted friction stir welding of 2.5 mm thick Al5052 aluminum alloy to 1.4 mm thick DP590 advanced high-strength steel plates are carried out. TIG-assisted Hybrid Friction Stir Welding process for joining dissimilar materials is optimized with its increased joint strength.

Comparing to the conventional FSW process, the HFSW process for dissimilar materials is optimized by varying TIG current. To investigate the effect of preheating source TIG, welding conditions were fixed as moving speed as 1 mm/sec, tool rotational speed as 400 RPM, tool offset as Al:St = 9:1, distance of tool to TIG 20 mm, and distance of TIG to interface 5 mm. Moreover, to investigate the mechanical characteristics of welded joints, evaluation of bead profiles, tensile test, Vickers hardness test were proceeded to compare the FSW and HFSW process. Compared to the FSW, which shows imperfect joint, HFSW showed perfect joint but significantly decreased effective thickness in HFSW 30 and 40 A by thinning effect. The maximum tensile strength was obtained in HFSW as 184 MPa (Joint efficiency: 84 %), which is 10 % increased value than that in FSW. Furthermore, IMC layer thickness is measured with SEM-EDS, and slightly increased IMC layer thickness in HFSW which is 0.7  $\mu\text{m}$  thicker than that in FSW is observed as the heat input increased, and it is also confirmed that the layer thickness satisfied below 10  $\mu\text{m}$  standard for application in the industrial fields. Consequently, the optimum conditions for sound joint strength in dissimilar butt welded joints of 2.5 mm Al5052 aluminum alloy and 1.4 mm DP590 high strength steel is TIG current of 20 A among 0, 20, 30, and 40 A.

In Chapter III, a comparative study in joining of dissimilar materials by FSW and HFSW processes is performed to realize the effect of different welding parameters on the thermal characteristics of the welded joints, growth of IMC layer thickness in the joint interface, and the mechanical characteristics of the joints. The result of numerical analysis was fairly matched with experimental results. The result of the comparison indicates the established numerical approach is proper to be applied in simulation of joining dissimilar materials through TIG-assisted HFSW process.

As the sequence of the numerical analysis, a 3-dimensional heat transfer model is further developed to estimate the temperature distribution and temperature histories. An approach is proposed to predict the IMC layer thickness at the joint interface using numerically analyzed temperature histories, and is validated the same with experimentally measured results. Based on the results of the heat conduction analysis, measurement of temperature history of the joint interface and elastic-plastic analysis are proceeded for estimation of IMC layer thickness and investigation of residual stress and plastic strain of the dissimilar joints.

The solution domain was constructed considering welding parameters to predict the temperature histories as well as IMC layer thickness in FSW and HSW weldments of aluminum alloy to steel sheets. As a result of heat conduction analysis, heat conduction in the aluminum alloy side is wider than in the steel side due to higher heat conductivity of the aluminum alloy than that of the steel. The numerically computed result of temperature histories in FSW and HFSW were compared with experimentally measured results, and a fair agreement is confirmed. Compared to the estimated IMC layer thickness of FSW, whose thickness as 1.4  $\mu\text{m}$ , elevation of TIG current increases numerically computed IMC layer thickness as 2.3  $\mu\text{m}$  in HFSW 20 A. From the comparison of the estimated IMC layer thickness and corresponding experimentally measured, it is confirmed that the numerical results are reasonably accurate in comparison to the corresponding measured results. The maximum of welding residual stress component  $\sigma_{zz}$ , which is to the welding line direction generated in dissimilar materials hybrid welded joints is approximately 5 %

higher than that of conventional friction stir welded joints. However, the equivalent stress of dissimilar materials welded joints shows almost identical value as those of friction FSW process and HFSW process. The plastic strain,  $\varepsilon^P_{EQ}$ , of dissimilar joints of HFSW shows slightly higher maximum value than that of FSW as a gap of 0.035.

In this chapter, Chapter IV, knowledge obtained from each chapter is summarized. The reliability of TIG assisted hybrid friction welded joint is procured through the experimental study. Also, the possibility on the application of the approach to predict IMC layer thickness in the dissimilar materials (Al5052-DP590) joints by FSW and HFSW through numerical analysis has been established. The estimation of the Fe–Al IMC layer thickness along the joint interface is necessary to assess the joint strength in dissimilar light-weight materials welded joints, especially the joint of aluminum alloy to high-strength steel by solid state welding process. It is realized that the heat generation per unit length of the joint gives a significant effect on peak temperature and growth of IMC layer thickness. The methodology is expected to advance the development for quantitative model of the appropriate experimental setting in joining dissimilar materials (aluminum alloy to high strength steel).

## Reference

[1]	Bang H.S., Oh C.I., Ro C.S., Park C.S. and Bang H.S.. 2007. Analysis of Thermal and Welding Residual Stress for Hybrid Welded Joint by Finite Element Method. KWJS. 25. 565-570
[2]	www.europarl.europa.eu, Comparative study on the differences between the EU and US legislation on emission in the automotive sector, Study by EMIS Committee.
[3]	Kobuki. S., 2002. Mass reduction on vehicle. TOYOTA Technical Review. 52, 8-11
[4]	Sakuri, K., 2008. The latest trends in aluminium alloy sheets for automotive body panels. KOBELCO Technology Review. 28, 22-28
[5]	Zhili, Feng., 2006. Characterization of thermo-mechanical behaviors of advanced high strength steels (AHSS): task 2-weldability and performance evaluations of AHSS parts for automotive structures. Automotive Lightweighting Materials. 28, 206-218
[6]	Pouranvari, M., 2017. Critical assessment: dissimilar resistance spot welding of aluminium/steel: challenges and opportunities. Mater. Sci. Technol. 33, 1705-1712
[7]	Nagatsuka, K., Xiao, B., Wu, L., Nakata, S., 2018. Resistance spot welding of metal/carbon-fibre-reinforced plastics and applying silane coupling treatment. Sci. Technol. Weld. Join. 23, 181-186
[8]	Rathod, M.J., Kutsuna, M. (2004). Joining of aluminum alloy 5052 and low-carbon steel by laser roll welding. Welding Journal, 83: 16 – 26
[9]	Agudo, L., Eyidi, D., Schmaranzer, C.H., Arenholz, E., Jank, N., Bruckner, J., Pyzalla, A. R. (2007). Intermetallic Fe Al-phases in a steel/Al-alloy fusion weld. Journal of Materials Science, 42 (12): 4205 – 4214.
[10]	Chen, C.M., Kovacevic, R. (2004). Joining of Al 6061 alloy to AISI 1018 steel by combined effects of fusion and solid state welding. International Journal of Machine Tools and Manufacture, 44 (11): 1205 – 1214.
[11]	Casalino, C., Leo, P., Mortello, M., Perulli, P., 2017. Effects of laser offset and hybrid welding on microstructure and IMC in Fe-Al dissimilar welding. METALS-BASEL.7, No page number
[12]	Das, A., Shome M., Das, C.R., Goecke S.F., De, A. (2015). Joining of galvanized steel and aluminium alloy using controlled short circuiting gas metal arc welding process. Science and Technology of Welding and Joining, 20 (5): 402 – 408.



[13]	Das, A., Shome, M., Goecke S.F. De, A. (2017). Joining of aluminium alloy and galvanized steel using a controlled gas metal arc process. <i>Journal of Manufacturing Process</i> , 27: 179 – 187.
[14]	Coelho, R.S., Kosta, A., Santos, dos., J.F., Pyzalla, A.K. (2012). Friction-stir dissimilar welding of aluminium alloy to high strength steels: Mechanical properties and their relation to microstructure. <i>Materials Science Engineering: A</i> , 556: 175 – 183.
[15]	Bang, H.S., Bang, H.S., Jeon, G.H., Oh, I.H., Ro, C.S. (2012). Gas tungsten arc welding assisted hybrid friction stir welding of dissimilar materials Al6061-T6 aluminum alloy and STS304 stainless steel. <i>Materials &amp; Design</i> , 37: 48 – 55.
[16]	Kusuda, Y., 2013. Honda develops robotized FSW technology to weld steel and aluminum and applied it to a mass-production vehicle. <i>Industrial Robot: An International Journal</i> . 40, 208-212
[17]	Rai, R., De, A., Bhadeshia, H.K.D.H., DebRoy, T. (2011). Review: friction stir welding tools. <i>Science and Technology of Welding and Joining</i> , 16 (4): 325 – 342.
[18]	Buchibabu., V., Reddy, G.M., De, A., J. (2017). Probing torque, traverse force and tool durability in friction stir welding of aluminum alloys. <i>Journal of Materials Processing Technology</i> , 241: 86-92.
[19]	Yaduwanshi, D.K., Bag, S., Pal, S. (2014). Effect of preheating in hybrid friction stir welding of aluminum alloy. <i>Journal of Materials Engineering and Performance</i> , 23 (10): 3794 – 3803.
[20]	Yaduwanshi, D.K., Bag, S., Pal, S. (2016). Numerical modeling and experimental investigation on plasma-assisted hybrid friction stir welding of dissimilar materials. <i>Materials &amp; Design</i> , 92: 166 – 183.
[21]	Bang, H.S., Bang, H.S., Kim, H.S., Kim, J.H., Oh, I.H., Ro, C.S. (2010). A study on the weldability and mechanical characteristics of dissimilar materials butt joints by laser assisted friction stir welding. <i>Journal of Welding and Joining</i> , 28 (6): 678 – 683.
[22]	Atabaki, M. M., Nikodinovski, M., Chenier, P., Ma, J., Harooni, M., Kovacevic, R., 2014. Welding of aluminum alloy to steels: an overview. <i>J. Manuf. Sci. Prod.</i> 14, 59-78
[23]	Nasiri, A. M., Li. L., Kim, S. H., Zhou, Y., Weckman, D. C., Nguyen, T. C. 2011. Microstructure and properties of laser brazed magnesium to coated steel. <i>Weld. J.</i> 90, 211-219

[24]	Shahverdi, H. R., Ghomashchi, M. R., Shabestari, S., Hejazi, J., 2002. Microstructural analysis of interfacial reaction between molten aluminium and solid iron. <i>J. Mater. Process. Technol.</i> 124, 345-352
[25]	Watanabe, T., Takayama, H., Yanagisawa, A. (2006). Joining of aluminum alloy to steel by friction stir welding. <i>Journal of Materials Processing Technology</i> , 178 (1-3): 342 – 349.
[26]	Tanaka, T., Morishige, T., Hirata, T. (2009). Comprehensive analysis of joint strength for dissimilar friction stir welds of mild steel to aluminum alloys. <i>Scripta Materialia</i> , 61 (7): 756 – 759.
[27]	Liu, X., Lan, S., Ni, J. (2014). Analysis of process parameters effects on friction stir welding of dissimilar aluminum alloy to advanced high strength steel. <i>Materials &amp; Design</i> , 59: 50 – 62.
[28]	Liu, X., Lan, S., Ni, J. (2015). Thermal mechanical modeling of the plunge stage during friction-stir welding of dissimilar Al 6061 to TRIP 780 steel. <i>Journal of Manufacturing Science and Engineering – T ASME</i> , 137: 041001-1 – 041001-11.
[29]	Habibnia, M., Shakeri, M., Nourouzi, S., Givi, M.K.B. (2015). Microstructural and mechanical properties of friction stir welded 5050 Al alloy and 304 stainless steel plates. <i>The International Journal of Advanced Manufacturing Technology</i> , 76 (5-8): 819 – 829.
[30]	Wei, Y., Li, J., Xiong, J., Zhang, F. (2013). Effect of tool pin insertion depth on friction stir lap welding of aluminum to stainless steel. <i>Journal of Materials Engineering and Performance</i> , 22 (10): 3005 – 3013.
[31]	Murakami, T., Nakata, K., Tong, H., Ushio, M. (2003). Dissimilar metal joining of aluminum to steel by MIG arc brazing using flux cored wire. <i>ISIJ International</i> , 43 (10): 1596 – 1602.
[32]	Das, A., Shome M., Goecke S.F., De, A. (2016). Numerical modelling of gas metal arc joining of aluminium alloy and galvanised steels in lap joint configuration. <i>Science and Technology of Welding and Joining</i> , 21 (4): 303 – 309.
[33]	Crucifix, S., Rest, C., Mena, N.J., Jacques, P.J., Simar, A. (2015). Modelling thermal cycles and intermetallic growth during friction melt bonding of ULC steel to aluminium alloy 2024-T3. <i>Science and Technology of Welding and Joining</i> , 20 (4): 319 – 324.
[34]	Atabaki, M.M., Nikodinovski, M., Chenier, P., Ma, J., Harooni, M., Kovacevic, R., 2014. Welding of aluminum alloy to steels: an overview. <i>J. Manuf. Sci. Prod.</i> 14, 59-78
[35]	Kattner, U.R., 1990. In: binary alloy phase diagrams. Materials Park, OH: ASM International; 147

[36]	Zhang, W., Sun, D., Han, L., Gao, W., Qiu, X., 2011. Characterization of intermetallic compounds in dissimilar material resistance spot welded joint of high strength steel and aluminum alloy. <i>J. Manuf. Process.</i> 178, 342-349
[37]	Xu, L., Wang, L., Chen, Y.C., Robson, J.D., Prangnell, P.B., 2016. Effect of interfacial reaction on the mechanical performance of steel to aluminum dissimilar ultrasonic spot welds. <i>Metall. Mater. Trans. A-Phys. Metall Mater. Sci.</i> 47A, 334-346
[38]	Chen, H.C., Pinkerton, A.J., Li, L., Liu Z., Mistry, A.T., 2011. Gap-free fibre laser welding of Zn-coated steel on Al alloy for light-weight automotive applications. <i>Mater. Des.</i> 32, 495-504
[39]	Agudo, L., Eyidi, D., Schmaranzer, C.H., Arenholz, E., Jank, N., Bruckner, J., Pyzalla, A., 2007. Intermetallic FeAl <sub>3</sub> -phase in a steel/Al-alloy fusion weld. <i>J. Mater. Sci. Technol.</i> 42, 4205-4214
[40]	Springer, H., Kostka, A., Payton, E.J., Raabe, D., Kaysser-Pyzalla, Eggeler, G., 2011. On the formation and growth of intermetallic phase during interdiffusion between low-carbon steel and aluminum alloys. <i>Acta Mater.</i> 59, 1586-1600
[41]	Das, A., Shome, M., Goecke, S.F., De, A., 2017. Joining of aluminium alloy and galvanized steel using a controlled gas metal arc process. <i>J. Manuf. Process.</i> 27, 179-187
[42]	Chen, N., Wang, H.P., Carlson B.E., Sigler, D.R., Wang, M., 2018. Fracture mechanisms of Al/steel resistance spot welds in coach peel and cross tension testing. <i>J. Mater. Process. Technol.</i> 252, 348-361
[43]	Chen, N., Wang, H.P., Carlson B.E., Sigler, D.R., Wang, M., 2018. Fracture mechanisms of Al/steel resistance spot welds in coach peel and cross tension testing. <i>J. Mater. Process. Technol.</i> 252, 348-361
[44]	Watanabe, T., Sakuyama, H., Yanagisawa, A., 2009. Ultrasonic welding between mild steel sheet and Al-Mg alloy sheet. <i>J. Manuf. Process. Technol.</i> 209, 5475-5480
[45]	Watanabe, T., Takayama, H., Yanagisawa, A., 2006. Joining of aluminum alloy to steel by friction stir welding. <i>J. Manuf. Process. Technol.</i> 178, 342-349
[46]	Ramachandran, K.K., Murugan, N., Shashi Kumar, S., 2015. Friction stir welding of aluminum alloy AA5052 and HSLA steel. <i>Weld. J.</i> 94, 291-300
[47]	Ramachandran, K.K., Murugan, N., Shashi Kumar, S., 2015. Effect of tool axis offset and geometry of tool pin profile on the characteristics of friction stir welded dissimilar joints of aluminum alloy AA5052 and HSLA steel. <i>Mater. Sci. Eng. A-struct. Mater. Prop. Microstruct. Process.</i> 639, 219-233

[48]	Liu, X., Lan, S., Ni, J., 2014. Analysis of process parameters effects on friction stir welding of dissimilar aluminum alloy to advanced high strength steel. <i>Mater. Des.</i> 59, 50-62
[49]	Movahedi, M., Kokabi, A.H., Seyed Reihani, S.M., Najafi, H., 2012. Effect of tool travel and rotation speeds on weld zone defects and joint strength of aluminium steel lap joints made by friction stir welding. <i>Sci. Technol. Weld. Join.</i> 17, 162-167
[50]	Dehghani, M., Amadeh, A., Akbari Mousavi, S.A.A., 2013. Investigations on the effects of friction stir welding parameters on intermetallic and defect formation in joining aluminum alloy to mild steel. <i>Mater. Des.</i> 49, 433-441
[51]	Anand, D., Chen, D.L., Bhole, S.D., Andreychuk, P., Boudreau, G., 2006. Fatigue behavior of tailor (laser)-welded blanks for automotive applications. <i>Mater. Sci. Eng. A-struct. Mater. Prop. Microstruct. Process.</i> 420, 199-207
[52]	Feistauer, E.E., Bergmann, L.A., Barreto, L.S., Dos Santos, J.F., 2014. Mechanical behavior of dissimilar friction stir welded tailor welded blanks in Al-Mg alloys for marine applications. <i>Mater. Des.</i> 59, 323-332
[53]	Piccini, J.M., Svoboda, H.G., 2017. Tool geometry optimization in friction stir spot welding of Al-steel joints. <i>J. Manuf. Process.</i> 26, 142-154
[54]	ASTM E8M, 2001, ASTM International, USA.
[55]	Bag, S., De, A. (2010). Probing reliability of transport phenomena based heat transfer and fluid flow analysis in autogeneous fusion welding process. <i>Metallurgical and Materials Transactions A</i> , 41 (9): 2337 – 2347.
[56]	Sutton MA, Reynolds AP, Wang DQ, Hubbard CR, <i>J Eng Mater Tech</i> , 2002, pp.124-215.
[57]	Buchibabu, V., Reddy, G.M., De, A. (2017). Probing torque, traverse force and tool durability in friction stir welding of aluminum alloys. <i>Journal of Materials Processing Technology</i> , 241: 86 – 92.
[58]	Mehta, M., Arora, A., De, A., DebRoy, T. (2011). Tool geometry for friction stir welding—optimum shoulder diameter. <i>Metallurgical and Materials Transactions A</i> , 42 (9): 2716–2722.
[59]	Kajihara, M. (2006). Quantitative evaluation of interdiffusion in Fe <sub>2</sub> Al <sub>5</sub> during reactive diffusion in the binary Fe–Al system. <i>Materials Transactions</i> , 47 (6): 1480 – 1484.
[60]	Sierra, G., Peyre, P., Deschaux Beaume, F., Stuart, D., Fras, G., 2008. Steel to aluminium braze welding by laser process with Al12Si filler wire. <i>Sci. Technol. Weld. Join.</i> 13, 430-437.

[61]	Colegrove P, 2000, 2nd Int. Symp. on Friction Stir Welding (Gothenburg, Sweden)
[62]	J H Hattel, HNB Schmidt and C.Tutum, Thermomechanical Modelling of Friction Stir Welding, Proc of the 8th Int Conf., Georgia, USA (2008), pp. 1-10.
[63]	Lockwood. W. D, Tomaz. B and Reynolds. A.P 2002 Mechanical response of friction stir welded AA2024: experiment and modeling Mater. Sci. Eng. A 323, pp. 348-53
[64]	Numerical simulation thermal history and residual stress in FSW of Al2014-T6, N.Rajamanickam, V.Balusamy, P.R.Thyla and G.hari Vignesh, Journal of scientific and industrial research, Vol 68, March 2009, pp. 192-198.
[65]	Mehta, M., Chatterjee, K., De, A. (2013). Monitoring torque and traverse force in friction stir welding from input electrical signatures of driving motors. Science and Technology of Welding and Joining, 18 (3): 191 – 197.